

Universidade de Lisboa
Faculdade de Ciências
Departamento de Física



**Dual tuned $^{19}\text{F}/^1\text{H}$ Multichannel Coil for Magnetic Resonance
Imaging of Human Knee at 7.0 Tesla**

Yiyi Ji

Dissertação

Mestrado Integrado em Engenharia Biomédica e Biofísica
Perfil em Engenharia Clínica e Instrumentação Médica

2013

Universidade de Lisboa
Faculdade de Ciências
Departamento de Física



**Dual tuned $^{19}\text{F}/^1\text{H}$ Multichannel Coil for Magnetic Resonance
Imaging of Human Knee at 7.0 Tesla**

Yiyi Ji

Dissertação

Mestrado Integrado em Engenharia Biomédica e Biofísica
Perfil em Engenharia Clínica e Instrumentação Médica

Orientador interno: Professor Doutor Alexandre Andrade

Orientador externo: Professor Doutor Thoralf Niendorf

2013

RESUMO

Anti-inflamatórios não esteróides (NSAIDs) tópicos foram introduzidos no tratamento da artrite reumatóide, de forma a evitar os efeitos secundários da administração oral destes medicamentos. Embora seja conhecido que os NSAIDs de aplicação tópica são capazes de penetrar na pele humana, não existem estudos com humanos *in vivo* que mostrem a eficiência de penetração e o percurso do medicamento até ao local de inflamação.

O *in vivo tracking* do medicamento deve ser efectuado por um método eficaz e não invasivo. A ressonância magnética (MRI) e espectroscopia por ressonância magnética (MRS) do flúor (^{19}F) são de maior interesse para este propósito, dado que a MRI oferece um excelente contraste de tecidos, elevada resolução espacial e temporal e, a ausência de flúor nos tecidos biológicos faz do núcleo deste átomo um *probe* ideal para fazer *tracking* e quantificação *in vivo* de NSAIDs que contenham flúor.

A baixa resolução espacial e temporal de ^{19}F MRI/MRS, devido a baixas concentrações deste átomo nas regiões de interesse, pode ser aumentada nos campos magnéticos ultra elevados (UHF) pelo aumento da razão sinal-ruído (SNR) que acompanha o aumento da intensidade do campo do magneto estático. Porém, o aumento do campo magnético acarreta desvantagens como o aumento da não homogeneidade do campo de excitação B_1^+ e da absorção da energia de radio frequência (RF), que causa o aquecimento indesejável dos tecidos. RF *array coils* de superfície com um design ideal e com os parâmetros RF refinados podem usufruir da elevada SNR de UHF e, ao mesmo tempo reduzir a não homogeneidade do B_1^+ e evitar a elevada deposição de energia de RF de modo a que esta não exceda os limites de taxa de absorção específica (SAR).

Neste projecto foi desenvolvida uma *coil* de superfície de frequência dual (^1H e ^{19}F) para registo de imagens anatómicas com protões, assim como de imagens e espectroscopia de flúor no *tracking* e quantificação deste átomo num creme de NSAID com flúor (ácido flufenâmico) num joelho humano a 7.0 Tesla.

A *coil* construída consiste em três partes, contendo quatro canais de protão e quatro canais de flúor, que abrangem toda a área de interesse. As duas partes anteriores, com dois canais

de flúor e um de protão cada, cobrem a parte anterior do joelho, onde o creme de NSAID é aplicado. A parte posterior, formada por dois canais de protão, é curvada convexamente para suportar confortavelmente o joelho durante os exames de MRI.

O circuito do condutor da *coil* foi imprimido numa folha de cobre através de um sistema de controlo numérico por computador. Vários condensadores foram soldados ao longo do condutor de modo a diminuir o seu comprimento, assim são evitadas as fases zero da onda sinusoidal, onde não há sinal, na medida em que o comprimento de onda em 7.0 T é aproximadamente o comprimento dos condutores. Foram colocados condensadores ajustáveis nos locais de circuito reservados ao *tuning*, *matching* e *decoupling* dos elementos da *coil*. Desde modo, a *coil* pode ser ajustada a diferentes *loads* (fantomas ou humanos) conforme o necessário. Além disso, ainda foram colocadas *cable traps* nos cabos de alimentação de cada canal, para evitar as correntes instáveis dos respectivos cabos que podem influenciar a performance da *coil*.

A performance da *coil* foi avaliada através de *S-parameters*, mais especificamente através do coeficiente de reflexão (S_{ii}), que indica a porção da energia que é reflectida quando ela é imposta no canal i , e através do coeficiente de transmissão (S_{ij}), que indica que porção da energia imposta no canal i é transmitida e perdida para o canal j . Os resultados obtidos mostraram que os coeficientes de reflexão de todos os canais se encontravam abaixo de -30 dB, ou seja, na pior das hipóteses, apenas 0.1% da energia emitida para um canal é reflectida para trás, o que mostra que quase toda a energia é recebida pelos canais para produzir o campo de excitação B_1^+ . Os coeficientes de transmissão variavam entre -16 dB a -25 dB, revelando que as perdas de energia de um canal para outro podem de ser até 2.5%, ou seja, a perda não é significativa.

O factor Q também foi medido para verificar a performance da *coil*. A razão entre Q com *load* e Q sem *load* de todos os canais apresentou-se menor que 0.5. Este resultado mostra que o ruído vem maioritariamente do *load* e não do circuito da *coil* em si, o que é desejável, uma vez que nestas condições uma melhor razão sinal-ruído pode ser obtida.

A intensidade e a fase dos campos de radiofrequência variam dentro do objecto conforme a sua forma, permitividade e condutividade eléctricas. Em campos maiores que 3.0 T, o

comportamento das ondas electromagnéticas torna-se difícil de prever com métodos simples e quási-estáticos, tanto que é necessário recorrer à simulação completa de campos electromagnéticos. As simulações oferecem um conhecimento antecipado do comportamento de B_1^+ , assim como da deposição da energia RF nos tecidos, que é mais elevada nos campos magnéticos ultra elevados, como no caso de 7.0 T. Deste modo, o sobreaquecimento dos tecidos pode ser previamente visualizada e evitada.

Neste projecto, as simulações foram efectuadas com o software SEMCAD X que se baseia no método das diferenças finitas no domínio temporal (FDTD) para resolver as equações diferenciais de Maxwell.

De forma a mostrar a credibilidade das simulações, uma simulação da *coil* com um fantoma foi efectuada de modo a obter mapas de B_1^+ , usados para comparar os mapas de B_1^+ obtidos experimentalmente. Como resultado, os mapas simulados e medidos apresentavam uma semelhança significativa em termos qualitativos. Ao nível quantitativo, estes apresentavam uma diferença de $21.5 \pm 7.6\%$ para os canais de protão e de $47.8 \pm 9.2\%$ para os canais de flúor, apesar das correcções de perdas de energia em hardware nas medições. A diferença quantitativa nos canais de protão pode dever-se a perdas extras desconhecidas no scanner. A significativa diferença presente nos canais de flúor pode ser explicada pelo facto dos mapas experimentais serem obtidos na frequência de protão e extrapolados através dos *S-parameters*, uma vez que não existia nenhum fantoma que contivesse flúor no momento da experiência. Adicionalmente, os *S-parameters* foram adquiridos fora do scanner, sendo por isso apenas uma aproximação dos *S-parameters* reais durante as medições. Contudo, pode afirmar-se que a validação das simulações é credível pela significativa semelhança qualitativa dos mapas em todos os canais, e da semelhança quantitativa entre os canais de protão.

Os valores de SAR médio de 10 g, obtidos por simulação para as configurações de fase 3 utilizadas nos scans reais, foram encontrados como sendo 0.306 W/kg para a frequência de flúor (279.5 MHz) e 0.375 W/kg para a frequência de protão (297.0 MHz). Estes valores encontram-se muito abaixo do limite estabelecido pelas directrizes da IEC, 20.0 W/kg para as extremidades do corpo. É de notar também que, os valores de SAR obtidos pela

simulação não têm em conta as perdas de energia existentes na realidade, por isso, num scan real, o valor de SAR não iria exceder os valores simulados.

Os valores de T_1 e T_2 para o creme de NSAID com ácido flufenâmico a usar nas experiências *in vivo* foram encontrados através de espectroscopia, através da variação de TR para o T_1 e de TE para o T_2 . Foi também elaborada uma curva de concentração, onde para cada quantidade de creme de NSAID existe a correspondente intensidade de sinal.

As imagens de ressonância obtidas com a *coil* construída mostram um bom contraste e homogeneidade na área de interesse. A homogeneidade foi conseguida por uma sessão de B_1^+ *shimming in vivo*. A resolução espacial foi de $0.7 \times 0.7 \text{ mm}^2$ no plano e 5 mm para a espessura de fatia para imagens de protão e, de $2 \times 2 \text{ mm}^2$ no plano e 5 mm para a espessura de fatia para imagens de flúor.

Os estudos *in vivo* foram conduzidos em dois voluntários saudáveis, na ausência de voluntários com reumatóide artrite. Os voluntários aplicaram o creme que contém NSAID sobre o joelho. Foram efectuadas espectroscopias não-localizadas a intervalos regulares de modo a verificar a existência da alteração do sinal inicial que pudesse indicar a absorção do creme na pele. Os resultados, porém, não se mostraram conclusivos, uma vez que a espectroscopia efectuada abrangia as regiões no exterior e no interior do corpo. Foi efectuada, adicionalmente, uma espectroscopia localizada com o método SPECIAL dentro do joelho de um dos voluntários, após 172 minutos do primeiro scan, contudo nenhum sinal foi detectado. A inexistência do sinal pode dever-se à não penetração do creme na região onde o voxel SPECIAL foi colocado, ou contrariamente, ter ocorrido a penetração do creme mas numa quantidade demasiada baixa para poder ser detectada.

Nos trabalhos futuros, devem-se ser incluídos outros métodos para detecção do creme de NSAID *in vivo* com a *coil* desenvolvida, como espectroscopias localizadas dentro e fora do joelho, com tempos mais longos de scan, e com pacientes que tenham reumatóide artrite e voluntários saudáveis, de modo a comparar a eficiência da absorção do medicamento.

Palavras chave: MRI, campos magnéticos ultra elevados, RF coil, array coil de superfície, RF coil de dual frequência, imagiologia de ^{19}F , espectroscopia de ^{19}F , simulações de campos EM, SAR, Artrite Reumatóide, NSAIDs.

ABSTRACT

Topical non-steroidal anti-inflammatory drugs (NSAIDs) have been introduced to treat rheumatoid arthritis condition in order to avoid side effects from its oral form. Although it is known that topical NSAIDs are able to penetrate the human skin, no human *in vivo* studies were carried out to show the penetration efficiency and the drug delivering path at the site of inflammation.

In vivo drug tracking should be carried out by a non-invasive and effective method. A good candidate is fluorine (^{19}F) magnetic resonance imaging (MRI) and spectroscopy (MRS), since MRI offers excellent tissue contrast and high spatial and temporal resolutions. The absence of fluorine in biological tissue makes it an ideal probe to track and quantify fluorine containing NSAIDs *in vivo*.

In this project, a dedicated $^1\text{H}/^{19}\text{F}$ dual tuned surface coil with eight channels was constructed to register proton anatomical images and fluorine images/spectroscopy to track and quantify a fluorine containing NSAID ointment in human knee at 7.0 tesla. The constructed coil showed low reflection and transmission coefficients (<-30 dB and <-16 dB respectively) and noise dominant Q ratio, which enounces SNR gain.

Electromagnetic field (EMF) simulations were carried out to visualize RF field patterns and SAR values for safety. Comparison between simulated and measured B_1^+ maps showed reasonable qualitative and quantitative agreement, validating the SAR simulations, which give an estimation of the deposited RF power in the tissue in a real MRI scan.

In vivo ^{19}F spectroscopy, aimed to observe and quantify the skin absorption of flufenamic acid contained NSAID, showed inconclusive results. The spectroscopy performed with a SPECIAL voxel placed inside the knee did not show any fluorine signal, either due to non-absorption of the NSAID or the absorbed quantity was too low to be detected. Further improved *in vivo* experiments should be carried out with RA patients.

Keywords: MRI, ultrahigh magnetic field, surface array RF coil, dual tuned RF coil, ^{19}F imaging, ^{19}F spectroscopy, EMF simulations, SAR, Rheumatoid Arthritis, NSAIDs.

ACKNOWLEDGEMENTS

This thesis would not have been possible without the help of many people and here I would like to express my gratitude.

First of all, I would like to express my gratitude to Professor Thoralf Niendorf and Dr. Sonia Waiczies for the opportunity to work at Berlin Ultrahigh Field Facility (B.U.F.F.), Max-Delbrück Center for Molecular Medicine (MDC), Berlin, Germany and especially for their encouragement, guidance and support.

I would like to thank Dr. Helmar Waiczies, who have been closely supervising my work. I highly appreciate his guidance, support and patience through this ultrahigh magnetic imaging experience, from which I have learnt a lot.

I'm very grateful to whole B.U.F.F. team which forms a very nice and cooperative work environment. A special thanks to Celal Özerdem, who has always been ready for my questions, to Andreas Gräßl, Matthias Dieringer and Lukas Winter for their help with many technical aspects of the coil.

I would like to thank all the professors of the Institute of Biophysics and Biomedical Engineering of the Faculty of Sciences of the University of Lisbon for their dedication and encouragement, without them this experience abroad would not have been possible. A special thanks to Professor Alexandre Andrade for his support and supervision.

I would like to thank my flat mates and also colleagues João Fernandes and João Periquito for their friendship, patience and joyful moments that we passed together in Berlin. I'm very grateful to Carolina Galvão who took the time to help me with my English.

At last but not at least, I would like to thank my family and all my friends for all their encouragement, support and love. To my parents, Zhengrong Ji and Weifen Xia, my brother Pusheng Ji, and Tiago Silva for their love, encouragement and support in my studies and decisions, and everything else they have given me over the years.

I dedicate this work to the memory of my grandfather Yongqing Ji, who taught me since little that the education is the best tool to achieve success.

CONTENTS

| | |
|---|------|
| RESUMO | i |
| ABSTRACT | v |
| ACKNOWLEDGEMENTS | vi |
| LIST OF FIGURES | x |
| LIST OF TABLES | xii |
| ABBREVIATIONS AND SYMBOLS | xiii |
| 1. INTRODUCTION..... | 1 |
| 1.1. Objective | 2 |
| 2. BACKGROUND..... | 3 |
| 2.1. Basics of Magnetic Resonance Imaging | 3 |
| 2.1.1. The Nuclear Spin..... | 3 |
| 2.1.2. Protons in a Static Magnetic Field | 5 |
| 2.1.3. Magnetic Resonance Signal | 6 |
| 2.1.4. Magnetic Resonance Imaging | 11 |
| 2.1.5. Basic Pulse Sequences | 14 |
| 2.2. MRI at Ultrahigh Fields | 18 |
| 2.3. Fluorine (^{19}F) imaging | 20 |
| 3. RADIOFREQUENCY (RF) COILS | 21 |
| 3.1. RLC circuit | 22 |
| 3.2. Tuning and Matching..... | 22 |
| 3.3. Decoupling..... | 23 |
| 3.4. Cable Trap..... | 24 |
| 3.5. Scattering-Parameters (S-Parameters) | 25 |
| 3.6. Quality factor | 27 |
| 4. MATERIALS AND METHODS | 28 |
| 4.1 Coil Construction..... | 28 |
| 4.1.1. Casing..... | 30 |

| | |
|--|----|
| 4.1.2. Cable trap | 30 |
| 4.2. Electromagnetic field (EMF) simulations..... | 31 |
| 4.2.1. Phantom simulation..... | 33 |
| 4.2.2. Human model simulation | 33 |
| 4.3. RF Bench analysis | 35 |
| 4.3.1. Tuning, Matching and Decoupling..... | 36 |
| 4.3.2. Q factor measurement | 36 |
| 4.4. Measurements | 36 |
| 4.4.1. Coil interface | 37 |
| 4.4.2. B_1^+ mapping | 38 |
| 4.4.3. Determination of T_1 and T_2 | 38 |
| 4.4.4. Calibration curve | 40 |
| 4.4.5. <i>In vivo</i> Imaging..... | 40 |
| 4.4.6. <i>In vivo</i> ^{19}F Spectroscopy | 40 |
| 5. RESULTS..... | 42 |
| 5.1. Coil Layout | 42 |
| 5.1.1. Cable traps..... | 43 |
| 5.2. RF Bench Analysis | 43 |
| 5.2.1. S-Parameters..... | 43 |
| 5.2.2. Q-factor | 45 |
| 5.3. Simulated and measured B_1^+ maps | 45 |
| 5.4. SAR evaluation | 48 |
| 5.5. T_1 measurement | 50 |
| 5.6. T_2 measurement | 52 |
| 5.7. Calibration Curve..... | 53 |
| 5.8. <i>In vivo</i> Imaging | 54 |
| 5.8.1. B_1^+ Shimming | 54 |
| 5.1.1. Proton and fluorine imaging..... | 56 |

| | | |
|------|---|----|
| 5.9. | <i>In vivo</i> ^{19}F Spectroscopy | 56 |
| 6. | DISCUSSION | 58 |
| 6.1. | Coil performance | 58 |
| 6.2. | B_1^+ mapping comparison | 59 |
| 6.3. | SAR evaluation | 61 |
| 6.4. | T_1 , T_2 and concentration curve..... | 61 |
| 6.5. | <i>In vivo</i> imaging and ^{19}F spectroscopy | 61 |
| 7. | CONCLUSION | 63 |
| 8. | REFERENCES..... | 64 |

LIST OF FIGURES

| | |
|--|----|
| Figure 1 – The nuclear spin | 3 |
| Figure 2 – The behavior of the nuclear spin in the absence and in the presence of an external magnetic field | 5 |
| Figure 3 - Precession of a nuclear magnetic moment about an externally applied magnetic field | 6 |
| Figure 4 – Behavior of the net magnetization vector in the presence of B1+ field..... | 7 |
| Figure 5 – Spin-lattice and spin-spin relaxations. | 8 |
| Figure 6 – T ₁ and T ₂ relaxation times | 9 |
| Figure 7 – The signal processing chain in an NMR experiment | 10 |
| Figure 8 – Magnetic field gradients' influence on main static field strength..... | 11 |
| Figure 9 – An illustration of slice selection..... | 12 |
| Figure 10 – Spatial encoding: phase encoding and frequency encoding..... | 13 |
| Figure 11 – K-space and correspondent reconstructed images by 2D Fourier transform ... | 14 |
| Figure 12 – Free induction decay | 15 |
| Figure 13 – T ₁ recovery curve by repeating 90° RF pulses. | 15 |
| Figure 14 – Spin echo sequence | 16 |
| Figure 15 - Spin echo signal and exponential decay | 16 |
| Figure 16 – Gradient echo sequence..... | 17 |
| Figure 17 – Effects of RF field inhomogeneities on MRI..... | 19 |
| Figure 18 – An RLC resonant circuit in series | 22 |
| Figure 19 – Equivalent serial RLC circuit of an MRI coil with tuning-matching circuit ... | 23 |
| Figure 20 – Element coupling and frequency shift | 23 |
| Figure 21 – Decoupling capacitor C _D | 24 |
| Figure 22 – Coaxial cable – cut away view..... | 25 |
| Figure 23 – A two-port component with transmitted and reflected waves a_i and b_i | 25 |
| Figure 24 – S-parameters of a coil with 2 elements at 297 MHz | 26 |
| Figure 25 – ¹ H/ ¹⁹ F dual tuned knee coil overview | 28 |
| Figure 26 – Illustration of the anterior parts of coil | 29 |
| Figure 27 – Illustration of the posterior part of the coil | 29 |
| Figure 28 – Cable trap used in the coil | 30 |

| | |
|---|----|
| Figure 29 – Simulation steps | 31 |
| Figure 30 – ADS circuit design environment..... | 32 |
| Figure 31 – ADS S-parameter visualization environment..... | 32 |
| Figure 32 – The EMF simulation model of the phantom with the coil | 33 |
| Figure 33 – Voxelized lower member of “Duke” with the coil..... | 34 |
| Figure 34 – ZVT8 (Rhode & Schwarz GmbH & Co. KG, Munich, Germany) | 35 |
| Figure 35 – 7.0 T whole-body scanner (Siemens Healthcare, Erlangen, Germany) | 36 |
| Figure 36 – Tx/Rx switch box | 37 |
| Figure 37 – 1 to 4 power splitter | 37 |
| Figure 38 – Coil interface box specialized for 1H/19F dual tuned knee coil | 37 |
| Figure 39 – ¹⁹ F GRE image of a sample filled with NSAID ointment..... | 39 |
| Figure 40 – SPECIAL voxel placement inside the knee | 41 |
| Figure 41 – Coil elements numbering | 42 |
| Figure 42 – PCB circuit and capacitors of the coil..... | 42 |
| Figure 43 – Placement of the coil in its casing on a volunteer | 42 |
| Figure 44 – Print of VNA screen while measuring S-parameters for left anterior part of the coil | 44 |
| Figure 45 – Print of VNA screen while measuring S-parameters for left anterior part of the coil | 44 |
| Figure 46 – Print of VNA screen while measuring S-parameters for right anterior part of the coil | 45 |
| Figure 47 – Relative B1 map of simulation and measurement..... | 46 |
| Figure 48 – 10 g averaged SAR distribution at 279.5 MHz for phase setting 3 | 49 |
| Figure 49 - 10 g averaged SAR distribution at 297.0 MHz for phase setting 3 | 50 |
| Figure 50 – Fitted T ₁ recovery curve from acquired data..... | 51 |
| Figure 51 – Fitted T ₂ recovery curve from acquired data..... | 53 |
| Figure 52 – Concentration curves for 100% NSAID ointment and for 50% NSAID ointment + 50% fluorine free ointment | 54 |
| Figure 53 – GRE images of a knee using different phase setting..... | 55 |
| Figure 54 – Destructive interference of RF field and its correction | 55 |
| Figure 55 – High resolution proton and fluorine images..... | 56 |
| Figure 56 – <i>In vivo</i> spectroscopy graphic results | 57 |
| Figure 57 – B ₁ ⁺ map of channel 1 and maximum value correction..... | 60 |

LIST OF TABLES

| | |
|--|----|
| Table 1 – Spin, gyromagnetic ratio, isotopic composition and abundance in biological tissues of some elements of mr interest | 4 |
| Table 2 – RF wavelength in air and in water for proton at different field strengths | 18 |
| Table 3 – ICE and FDA guidelines for SAR and heating in human MRI studies..... | 19 |
| Table 4 – Capacitors used for cable traps..... | 43 |
| Table 5 – S_{ii} and S_{ij} of the coil elements | 43 |
| Table 6 – Q_l , Q_{ul} and Q_l/Q_{ul} of each coil channels. | 45 |
| Table 7 – Correction factors of measured B_1^+ maps | 47 |
| Table 8 – Simulated and measured b_1^+ values and their comparison. | 48 |
| Table 9 – Peak averaged SAR at 279.5 MHz and 297.0 MHz | 48 |
| Table 10 – The phase and amplitude of worst case SAR at ^{19}F and ^1H frequencies | 49 |
| Table 11 - Signal magnitude of spectroscopies of 100% NSAID ointment sample and 50% NSAID ointment + 50% fluorine free ointment sample at different TRs..... | 51 |
| Table 12 - Signal magnitude of spectroscopies of 100% NSAID ointment sample and 50% NSAID ointment + 50% fluorine free ointment sample at different TEs..... | 52 |
| Table 13 - Signal magnitude of spectroscopies and amount of flufenamic acid present at different SPECIAL voxel sizes for 100% NSAID ointment sample | 53 |
| Table 14 - Signal magnitude of spectroscopies and amount of flufenamic acid present at different special voxel sizes for 50% nsaid ointment + 50% fluorine free ointment sample..... | 53 |
| Table 15 – Phase settings for B_1^+ homogeneity experiment. | 54 |
| Table 16 – <i>In vivo</i> ^{19}F spectroscopy of applied fluorine containing topical NSAID ointment. | 57 |

ABBREVIATIONS AND SYMBOLS

γ – Gyromagnetic ratio

$\vec{\mu}$ – Magnetic moment

ω – frequency (rads/s), usually Larmor frequency

^1H – Proton

^{19}F – Fluorine

ADS – Advanced Design System

B_0 – External static magnetic field

B_1^+ – Excitation radio frequency field

EMF – Electromagnetic Field

FDA – Food and Drug Administration

FID – Free Induction Decay

FOV – Field of View

FWHM – Full Width at Half Maximum

GRE – Gradient Recalled Echo

IEC – International Electrotechnical Commission

$\vec{\text{M}}$ – Net magnetization

$\vec{\text{M}}_0$ – Thermal-equilibrium net magnetization

$\vec{\text{M}}_{\text{xy}}$ – Transversal component of net magnetization

$\vec{\text{M}}_{\text{z}}$ – Longitudinal component of net magnetization

MRI – Magnetic Resonance Imaging

MRS – Magnetic Resonance Spectroscopy

NMR – Nuclear Magnetic Resonance

NSAID – Non-Steroidal Anti-Inflammatory Drug

PCB – Printable Circuit Board

RA – Rheumatoid Arthritis

RF – Radio Frequency

ROI – Region of Interest

Rx – Receive

SAR – Specific Absorption Rate

SE – Spin Echo

S_{ii} – Reflection coefficient of S-parameter

S_{ij} – Transmission coefficient of S-parameter

SNR – Signal to Noise Ratio

SPECIAL – SPin ECho full Intensity Acquired Localized

T – Tesla

Tx – Transmit

UHF – Ultra High Field

VNA – Vector Network Analyzer

1. INTRODUCTION

Rheumatoid arthritis (RA) is an autoimmune disease that causes long-term joints and surrounding tissues inflammation. It affects usually joints on both sides of the body equally. Wrists, fingers, knees, feet, and ankles are the most commonly affected, though it can also affect another body parts such as eyes, mouth and lungs [1].

RA treatment includes non-steroidal anti-inflammatory drugs (NSAIDs), which are known for their anti-inflammatory, analgesic, antipyretic and antithrombotic effects [2]. Despite their beneficial proprieties for RA, conventional oral form of NSAIDs present side effects such as irritation and bleeding of gastrointestinal mucosa, heart burn and nausea, thus topical NSAIDs were introduced as an alternative to avoid these side effects and also to minimize the overall required dosage [3].

However, to be effective, topical NSAIDs have to penetrate the skin and reach the joints in a sufficient concentration. Although many studies have shown overall therapeutic active effects of topical NSAIDs [4–7] and effective skin penetration [8,9] it is still not shown how nor how much of the drug reaches the site of inflammation to exert their therapeutic effect. This *in vivo* drug tracking should be carried out by a non-invasive and effective method, and fluorine (^{19}F) magnetic resonance imaging (MRI) and spectroscopy (MRS) are of major interest.

MRI provides an excellent tissue contrast and high spatial and temporal resolutions, and the fluorine with a high gyromagnetic ratio and high signal sensitivity, about 83% of hydrogen's; together with its absence background in biological tissue [10] form an ideal probe to track and quantify NSAIDs *in vivo*. MRI at ultrahigh fields (7.0 T) benefits from the increased signal to noise ratio (SNR) which can be translated into higher spatial and temporal resolutions [11], which is of high interest of ^{19}F MRI and MRS due to low concentration of fluorine nuclei in region of interest [12].

But on the other hand, higher fields lead to more B_1^+ excitation field inhomogeneities and to more radio frequency (RF) power absorption, which can cause undesirable tissue heating [13]. RF surface array coils with an optimum design and refined RF parameters can get use

of the high SNR of the ultrahigh magnetic fields and at same time reduces the B_1^+ non-homogeneities and avoid high RF power absorption in order to stay within the limits of specific absorption rate (SAR). This limits are established by authority entities such as Food and Drug Administration (FDA) and International Electrotechnical Commission (IEC), concerning patient safety [14,15].

Typical approach for ^{19}F studies combines proton images containing anatomical information and fluorine images that contain study aimed information. This can be performed either by a single tuned RF coil, which can have a sufficient bandwidth to accommodate both nuclei or a smaller bandwidth that needs to be constantly tuned and matched between ^1H and ^{19}F frequencies, or by a dual tuned RF coil tuned and matched to both frequencies. Dual tuned RF coils are preferred rather than single tuned coils, since a large bandwidth needed to cover both frequencies of the later ones leads to significant noise increase and signal sensitivity drop, or in the other case, the constant manipulation between frequencies can change image registration between one nuclei scan to the other, besides, the sensitivity profile also varies from one frequency to the other [16].

1.1. Objective

The purpose of the present thesis is to develop a dual tuned array coil for proton and fluorine magnetic resonance imaging and spectroscopy at 7.0 T for human knee. The developed coil will be used to register ^1H anatomical images and ^{19}F images and spectroscopy to track and quantify a fluorine containing NSAID ointment (flufenamic acid (2- $\{[3\text{-(Trifluoromethyl) phenyl]amino}\}$ benzoic acid) *in vivo*).

2. BACKGROUND

2.1. Basics of Magnetic Resonance Imaging

Magnetic resonance imaging (MRI) is a relatively recent medical imaging modality as its first practical medical application was performed in 1973 [17]. It has shown to be a powerful imaging modality due to its flexibility and sensitivity to a wide range of tissue properties and most importantly to the noninvasive nature of the magnetic fields. MRI is based on the principle of Nuclear Magnetic Resonance (NMR) [18], which is explained below.

2.1.1. The Nuclear Spin

Nuclear Magnetic resonance is based upon the interaction between an applied external magnetic field and atoms that possess nuclear magnetic moment, or more generally referred as nuclear spin [15].

Protons and neutrons of nucleus possess intrinsic angular momentum as they rotate around an axis at constant rate. In classical-physics view, protons and neutrons can be regarded as rotating mass with charge, therefore giving rise to a magnetic moment which behaves like small magnets (Figure 1). A neutron has no net charge but it is composed of charged particles (two down-Quarks and one up-Quark) possessing an intrinsic spin of $1/2$ and therefore belongs to the group of Fermions, like the protons [19,20].

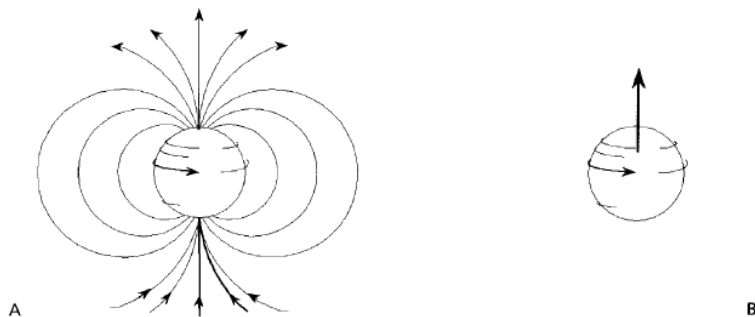


Figure 1 - A: A rotating proton or neutron can classically be represented with a dipole magnetic field. B: The magnetic moment vector indicates direction and magnitude of the magnetic field induced by a spinning proton or neutron and behaves like a small magnet. Adapted from [21].

Pairing phenomenon occurs within the nucleus, where the magnetic moments of proton-proton or neutron-neutron pairs tend to align in opposition canceling each other. Thus, nuclear spin can be zero if the nucleus has an even number of protons and neutrons which pair up, resulting in a zero net magnetic moment. Such nucleus does not interact with an external magnetic field. On the other hand, nuclear spin can be multiples of 1/2 if a nucleus has an odd number of protons or neutrons, in this case there are unpaired protons or neutrons that produce a non-zero net magnetic moment, and therefore this nucleus will interact with an external field [19,21,22]. Almost all atoms have at least one naturally occurring isotope that possesses spin, therefore nearly every element is examinable in MRI [15].

An important physical quantity for MRI is the ratio of the magnetic moment to the angular momentum, called gyromagnetic ratio (γ) [19]. Table 1 shows information about spin, gyromagnetic ratio, isotopic composition and abundance in biological tissues of some selected elements of the MRI interest. It is also notable that hydrogen has a very high concentration in the body, due to its presence in water, fat and other organic molecules, and a relatively high gyromagnetic ratio, which makes these nuclei, composed only by a single proton, the source of signal for nearly all clinical MRI exams. This fact leads to the general description of MRI effects made with term “proton” (also used in the next sections of this work), although these effects are same for other nuclei [19].

| Element | Symbol | Net Spin | γ (MHz/T) | Natural abundance | Biological abundance |
|------------|------------------|---------------|---------------------|----------------------|-------------------------|
| Hydrogen | ^1H | $\frac{1}{2}$ | 42.58 | 0.99985 | 0.63 |
| | ^2H | 1 | 6.54 | 0.00015 | |
| Fluorine | ^{19}F | $\frac{1}{2}$ | 40.08 | 1 | 0.00001 |
| Carbon | ^{13}C | $\frac{1}{2}$ | 10.71 | 0.11 | 0.094 |
| | ^{12}C | 0 | 0 | 0.89 | |
| Sodium | ^{23}Na | $\frac{3}{2}$ | 11.27 | 1 | 0.00041 |
| Phosphorus | ^{31}P | $\frac{1}{2}$ | 17.25 | 1 | 0.0024 |

Table 1 - Spin, gyromagnetic ratio (γ), isotopic composition and abundance in biological tissues of some elements of MR interest. Adapted from [22,23].

2.1.2. Protons in a Static Magnetic Field

Without an external magnetic field, protons spins in random directions, which results in a null net magnetic moment, also called net magnetization \vec{M} , illustrated in Figure 2 A. On the other hand, when the protons are placed inside a static magnetic field \vec{B}_0 , they experience two quantized energy states ($2 \times \text{spin} + 1$) with energy difference of ΔE , which is proportional to external magnetic strength. Protons in the lower energy level, called spin up, align parallel to \vec{B}_0 (conventionally set as z direction) and protons in the higher energy level, called spin down, align antiparallel to \vec{B}_0 , as shown in Figure 2 B. At thermal equilibrium state a number of protons in higher energy state transits to lower energy state by exchanging energy with their surroundings, and vice versa, but the mean number of protons in each energy state remains constant. The parallel alignment cancels out the antiparallel alignment, and as there are more protons in the lower energy state than in the higher energy state, the excess of parallel alignment results in a measurable net magnetization vector \vec{M}_0 aligned with \vec{B}_0 which is called thermal-equilibrium magnetization [19,21]. \vec{M}_0 increases proportionally with B_0 , and the MRI signal is directly proportional to \vec{M}_0 . This increase of signal with increase of B_0 explains one of the motivations for development of higher magnetic field systems [19].

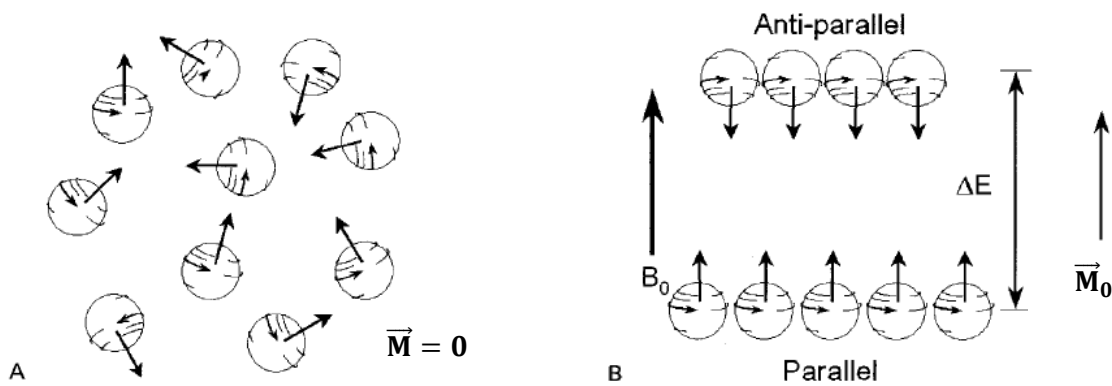


Figure 2 – A: in absence of an external magnetic field, nuclei spins are in random directions, resulting in a zero net magnetization. B: in presence of an external magnetic field \vec{B}_0 , protons align parallel (lower energy state) or antiparallel (higher energy state) to the \vec{B}_0 , the excess of parallel alignment results in a measurable net magnetization. Adapted from [21].

Besides magnetic alignment, an external magnetic field exerts a torque on the magnetic moment causing the proton to precess around z direction, as shown in Figure 3. The frequency of precession, also known as the Larmor frequency (ω_0), is proportional to the strength of \vec{B}_0 and is influenced by gyromagnetic ratio of the element. It is described by Larmor equation (Eq. 1) [15,19]:

$$\omega_0 = \gamma B_0 \quad \text{Eq. 1}$$

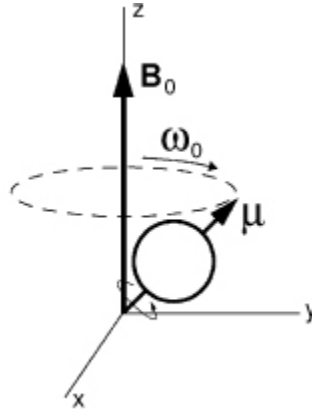


Figure 3 - Precession of a nuclear magnetic moment ($\vec{\mu}$) about an externally applied magnetic field with \vec{B}_0 with angular frequency of ω_0 [19].

2.1.3. Magnetic Resonance Signal

Excitation of the spins

At equilibrium, the longitudinal magnetization (aligned with \vec{B}_0) of \vec{M}_0 is maximal and is denoted as \vec{M}_z . However, compared to the strength of \vec{B}_0 , \vec{M}_z (in order of μT) is too small, making it impossible to be directly detected. Therefore, it is necessary to tip \vec{M}_0 into the transversal xy plane in order to gain a measurable signal [21].

To tip the thermal-equilibrium magnetization vector \vec{M}_0 , it is necessary to disturb the equilibrium state of the protons. This can be done by an additional time-varying magnetic field perpendicular to \vec{B}_0 , called \vec{B}_1 , through application of a radiofrequency (RF) excitation pulse at Larmor frequency on a transmit (Tx) RF coil. The generated \vec{B}_1 consists of two

circular polarized fields: \vec{B}_1^+ , which can excite the spin as it has the same sense of rotation as the precessing spins, and \vec{B}_1^- , which has an opposite direction of rotation and does not contribute for excitation, however it is decisive for signal reception.

Now \vec{M} (called \vec{M} instead of \vec{M}_0 once the system is no longer in equilibrium state) has to precess about \vec{B}_1 while continuing to precess at the same time about \vec{B}_0 , as result, in a stationary frame (x y z) \vec{M} will spiral towards xy plane as shown in Figure 4 A. In a rotating frame (x_{rot} y_{rot} z_{rot}), where z_{rot} (parallel to \vec{B}_0) is the axis of rotation, while x_{rot} and y_{rot} axes rotates at the Larmor frequency, \vec{M} will tip at an angle, the flip angle α , about x_{rot} and a transversal component of net magnetization \vec{M} , \vec{M}_{xy} , is originated, as can be observed in Figure 4 B [15,24].

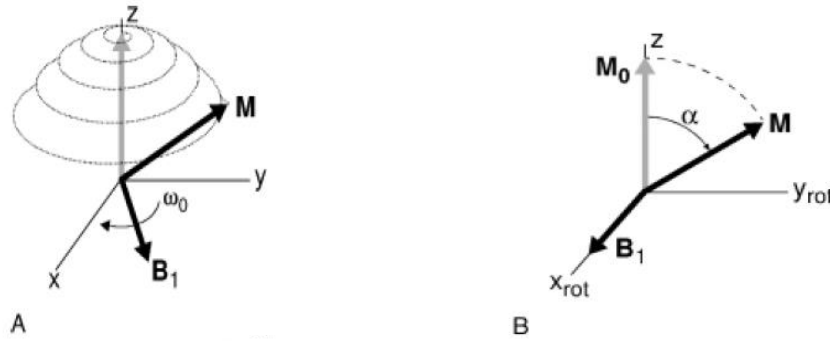


Figure 4 – Behavior of the net magnetization vector \vec{M} in presence of a circular polarized and perpendicular to \vec{B}_0 magnetic field \vec{B}_1 in A) a stationery frame and on B) a rotational frame. [19]

The flip angle α depends on the gyromagnetic ratio (γ), the strength of \vec{B}_1 and on the duration τ of the RF field, as described by the following equation [19]:

$$\alpha = \gamma B_1 \tau \quad \text{Eq. 2}$$

By an appropriate choice of B_1 and τ any flip angle α can be obtained. A 90° flip angle is caused by a 90° pulse, also called an excitation pulse, and moves the net magnetization from longitudinal axis into transverse plane. The RF pulse also induces phase coherence to all individual spins, that is why the net magnetization vector can have a transverse component in non-equilibrium conditions [17].

Relaxation

When the RF pulse is turned off, \vec{B}_1 vanishes and the relaxation occurs as the protons return to equilibrium state. This process is called free induction decay (FID). The relaxation can be divided into spin-lattice relaxation and spin-spin relaxation. In the first one, the longitudinal component of \vec{M} becomes \vec{M}_0 again, and in the latter one, the transverse component of \vec{M} returns to zero [17], as shown in Figure 5.

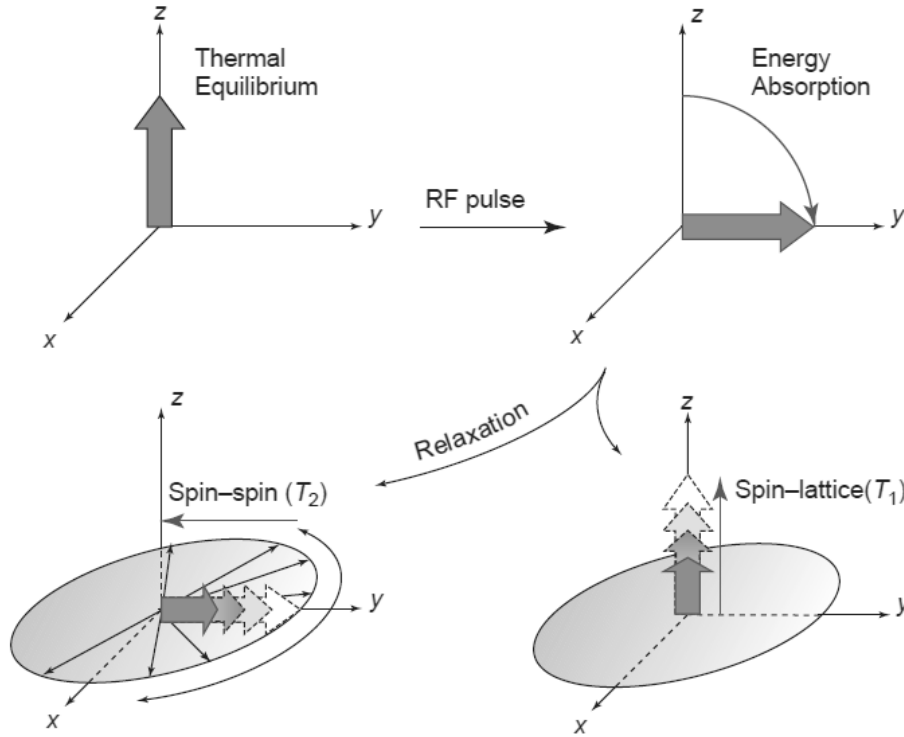


Figure 5 – schematic overview of free induction decay process. The RF pulse creates a net transverse magnetization due to energy absorption and phase coherence. After RF pulse, spin-lattice and spin-spin relaxations occur [17].

Spin-lattice relaxation

In the absence of \vec{B}_1 , the previous excited protons, in order to return to the lowest energy state, tends to re-align their magnetic moment to \vec{B}_0 . Therefore the longitudinal component of \vec{M} becomes maximum again, thus the spin-lattice relaxation is also called longitudinal relaxation. The energy difference is transferred to the lattice of nearby atoms and is transformed into heat. The process of this relaxation can be described by follow equation.

$$M_z(t) = M_z(t=0)\cos\alpha e^{-t/T_1} + M_0(1 - e^{-t/T_1}) \quad \text{Eq. 3}$$

where $M_z(t)$ is the longitudinal component of net magnetization vector $\vec{M}(t)$, $M_z(t=0)\cos\alpha$ is the value of longitudinal component immediately after RF pulse and T_1 is the spin-lattice relaxation time – the time taken for the net magnetization to recover to 63% of M_0 or $M_0(1 - e^{-1})$ – which differs from tissue to tissue and increases with the strength of \vec{B}_0 [11,17].

Spin-spin relaxation

Physically, each spin vector experiences a slightly different magnetic field because of the different chemical environment. As a result of these spin–spin interactions, the spins rotate at slightly differing angular frequencies, which results in a loss of the phase coherence and a decrease of the transverse component $M_{xy}(t)$. This spin-spin relaxation, also called transversal relaxation, is described by

$$M_{xy}(t) = M_{xy}(t=0) \sin\alpha e^{-t/T_2} \quad \text{Eq. 4}$$

where $M_{xy}(t=0) \sin\alpha$ is the value of the transverse component immediately after the RF pulse, and T_2 – the spin-spin relaxation time – takes place when $M_{xy}(t)$ has decayed to 37% of its original value or $M_{xy}(t=0)e^{-1}$ and it depends considerably on the tissue. In this mechanism of dephasing, no energy is lost, but since it also includes the spin-lattice interaction related to T_1 , T_2 has to be shorter than T_1 , and it is rather independent of B_0 [11,17].

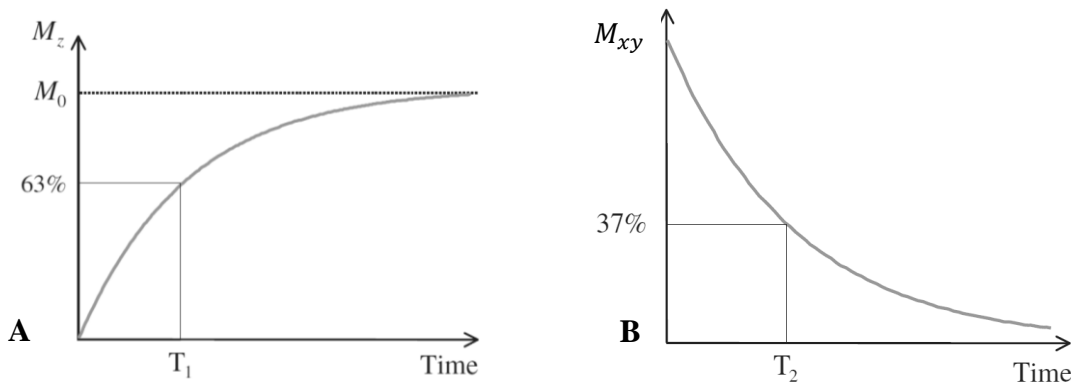


Figure 6 – A: The longitudinal relaxation and relaxation time T_1 . B: The transversal relaxation and relaxation time T_2 . [8]

The longitudinal and transversal relaxations are illustrated in Figure 6, with their correspondent relaxation times.

There is an additional dephasing caused by \vec{B}_0 inhomogeneities which contributes to an even faster signal decay. This type of decay occurs with the time constant T_2^* , typically shorter than T_2 [20].

Signal reception

By placing a receive (Rx) RF coil near to the sample, the precessing transversal magnetization $M_{xy}(t)$ will induce an alternating voltage at the ends of the loop due to Faraday's Law of induction. The intensity of the detected signal is connected to the magnetic field of the loop via the principle of reciprocity [25,26].

After its detection, the signal is first amplified and then mixed with a frequency Ω , which slightly differs from Larmor frequency. After the demodulation, the signal is sampled by an Analogue-Digital-Converter (ADC) and finally transferred to the computer for post-processing, as illustrated in Figure 7 [18].

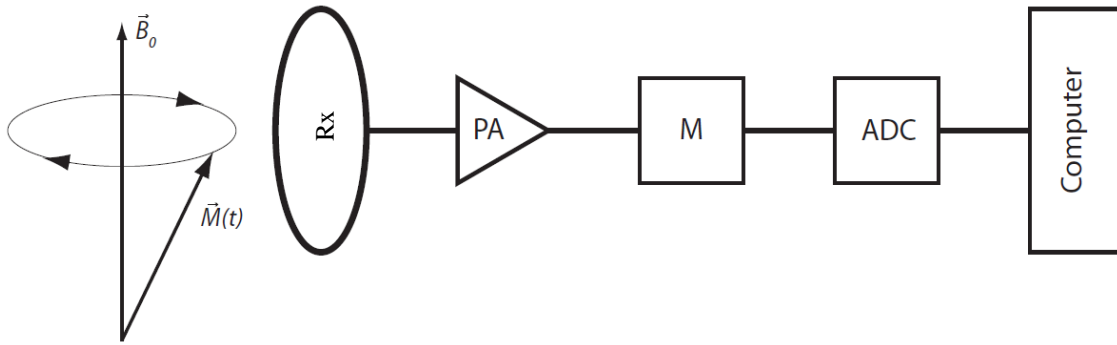


Figure 7 – Block diagram of the signal processing chain in an NMR experiment with PA being the power amplifier, M the mixer for demodulation and ADC the Analogue-Digital-Converter [18].

2.1.4. Magnetic Resonance Imaging

Magnetic resonance imaging is based on determination of spatial location of NMR signals to create an image. This is possible by introduction of magnetic field gradients that produce a small variation on the strength of the main magnetic field \vec{B}_0 [15].

Magnetic Field Gradients

Magnetic field gradients consist of three magnetic fields that add or subtract a small amount of field strength from the main static magnetic field \vec{B}_0 , linearly proportional to the distance from the isocenter in x, y and z direction. This spatial variation of the strength of \vec{B}_0 results on different Larmor frequencies on protons located at different positions along the applied gradient in a known way, as shown in Figure 8 [19].

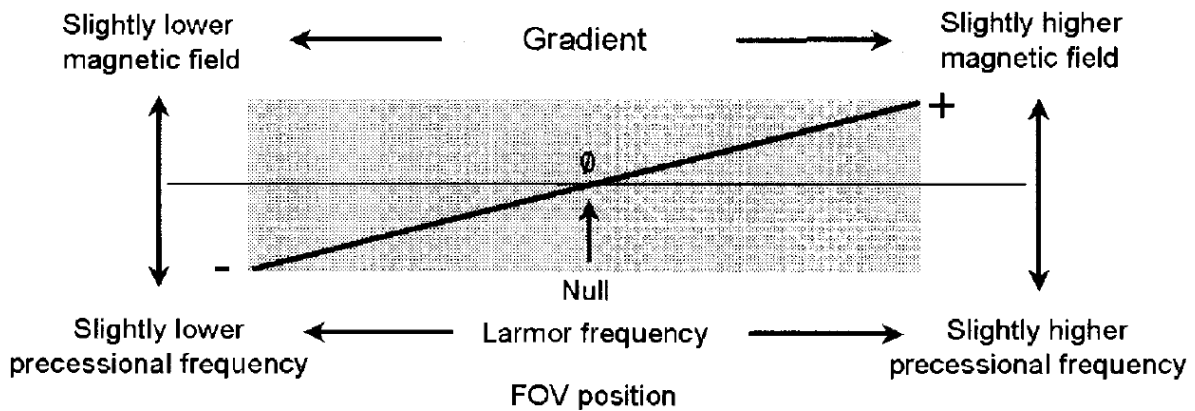


Figure 8 – Total magnetic field strength along position when a magnetic gradient field is applied to the main static field. This variation causes protons in different positions to spin at different but known Larmor frequencies [21].

Slice Selection

The first step to acquire a MRI image is the slice selection. The slice-select gradient (G_{SS}) creates a linear correspondence between the Larmor frequency and the position, a desired slice can be obtained by applying an RF pulse with selected center frequency (ω_c), thus, only the protons in the position corresponded to center frequency (z_c), called slice position, can be excited, as shown in Figure 9 [19].

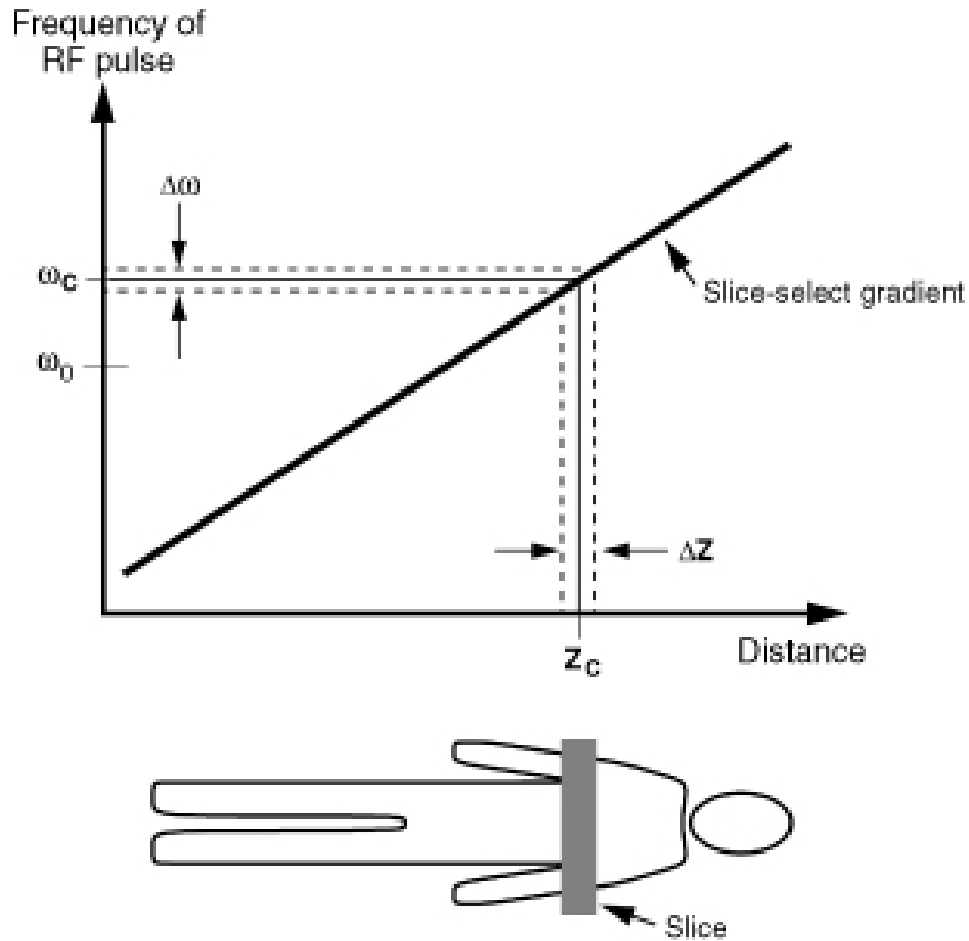


Figure 9 – An illustration of slice selection [19].

Spatial encoding

After the slice selection, e.g., in z direction, all the protons within the slice precess at same frequency. To obtain an image from it, it is necessary to proceed spatial encoding. Spatial encoding comprises two steps, phase encoding and frequency encoding [20,24].

For phase encoding, a gradient in y direction is switched on immediately after the RF pulse of the slice selection and before the signal acquisition. This gradient modifies the Larmor frequency of the protons along y direction (Figure 10 A). As result, the protons in a higher field strength gain phase relative to the protons in a lower field strength. In this way, each line of protons within the slice can be identified by its unique phase.

For frequency encoding, a frequency-encoding gradient is applied in x direction during acquisition time. This gradient causes different Larmor frequencies of the protons along x-axis, thus each column of protons within the slice can be characterized by its specific frequency (Figure 10 B).

In this way, each volume element (voxel) of the slice will have unique frequency and phase allowing its spatial identification.

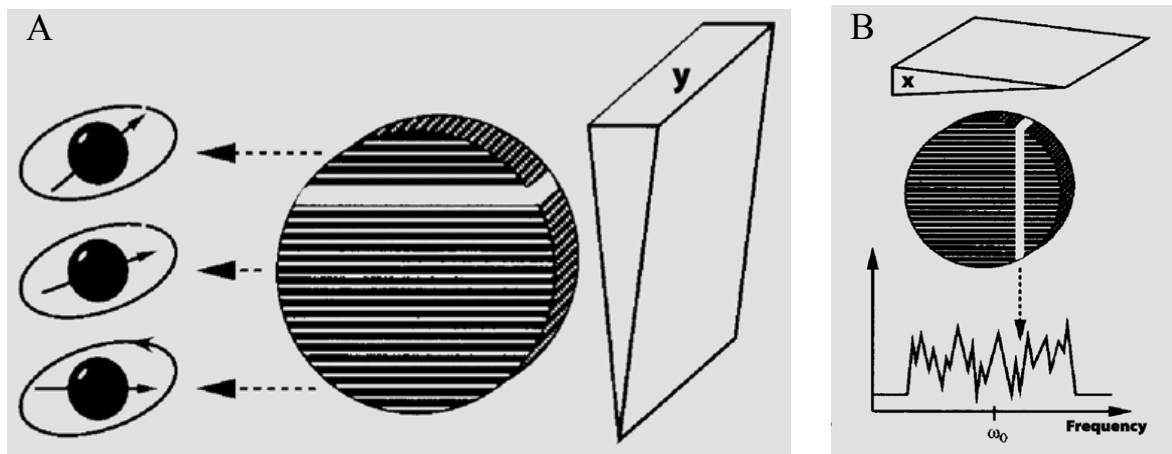


Figure 10 – Spatial encoding. A: Phase encoding – a y-gradient causes unique phase shifts within lines of the selected slice. B: Frequency encoding – an x-gradient causes specific Larmor frequencies within columns of the selected slice. [20]

K-space

K-space is where the collected encoded data from the MR signals are stored, corresponding to the inverse Fourier transform of the image space. It has two axes, the horizontal axis k_x stores the frequency information, and the vertical axis k_y stores the information about the phase. Each k-space line corresponds to one measurement and it is acquired for each phase-encoding step. An MR image is created from raw data by application of 2D Fourier transform after the scan is over and k-space is filled.

K-space lines do not correspond to the resulting image lines. Rather, the data from center of k-space mainly determines contrast in the image while the outer lines primarily contain spatial information (Figure 11). [20]

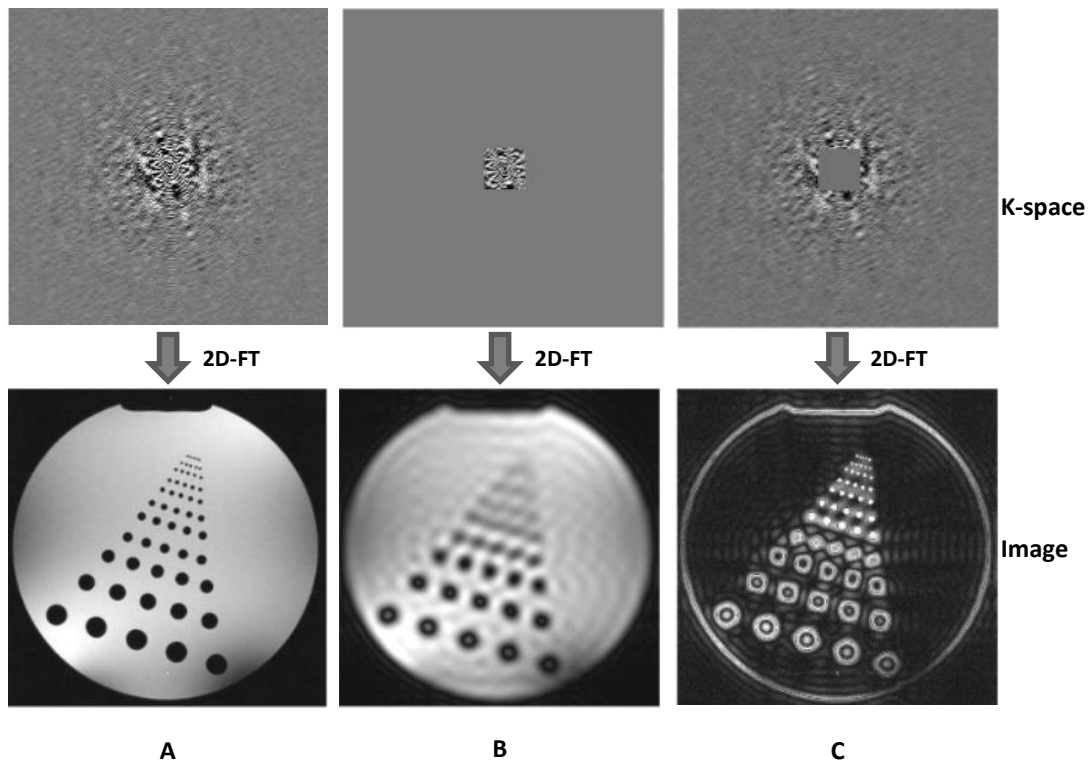


Figure 11 – K-space and correspondent images by 2D Fourier transform (FT) of k-space. A: reconstruction from full k-space, B: reconstruction from only the centre of k-space results in an image with good contrast but lacking in detail, C: reconstruction from only the edges of k-space results in an image where only the edges and detail of the imaged object. [15]

2.1.5. Basic Pulse Sequences

A pulse sequence is a set of RF pulses applied to a sample to produce a specific form of NMR signal [22].

One pulse sequence

A single 90° RF pulse is applied uniformly to the sample in an associated static magnetic field and the net magnetization is tipped into the transverse plane. After the pulse, as the spins begin to realign themselves and return to equilibrium orientation in z-direction, the net magnetization begins to precess freely about \vec{B}_0 , emitting energy. This energy is captured, resulting in an MR signal known as free induction decay (FID). The initial

magnitude of FID signal depends on the value of M_0 prior to the 90° RF pulse. The FID decays with time as relaxation occurs [15].

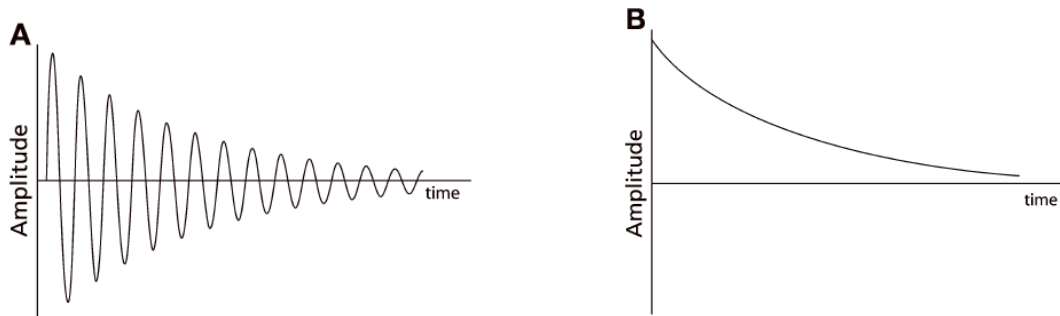


Figure 12 – Free induction decay. A: oscillating FID recorded within stationary frame of reference. B: non-oscillating FID recorded within rotating frame of reference. [24]

The FID experiment is used in MR spectroscopy where different nuclei with different Larmor frequencies can be differentiated within a sample [18].

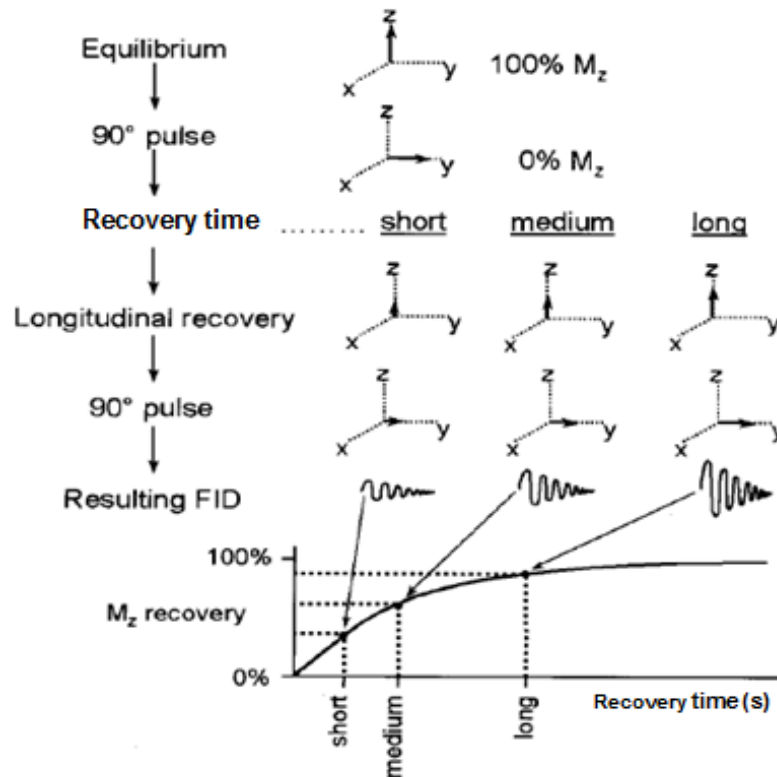


Figure 13 – T_1 recovery curve by repeating 90° RF pulses [21].

Additionally, repeated 90° pulses can be conducted to determine T_1 time. The initial 90° pulse, which takes the M_z to zero, is followed by a recovery time and then a second 90° pulse is applied to examine the longitudinal recovery by displacing it into the transverse plane. By repeating the sequence with different repetition times (TR) a T_1 recovery curve – $M_o(1 - e^{-TR/T_1})$ – can be determined and T_1 value can be estimated [18,21], as shown in Figure 13.

Spin Echo (SE) sequence

In spin echo sequence, a 90° RF pulse is first applied to rotate the net magnetization into the transversal plane. After this pulse, dephasing occurs as the precessing of some spins are faster than others due to \vec{B}_0 inhomogeneities. Faster spins acquire positive phase (running clockwise), while slower ones lag behind and acquire negative phase (running counterclockwise). Dephasing occurs during the first half echo time (TE), then a 180° RF pulse is delivered to reverse or refocus the spins. As consequence the spins that were ahead before are now behind and vice versa, only the spins that are now behind will catch up as their respective speeds remain the same. Thus, after second half TE all spins will meet once again in phase forming the echo signal [20,24], Figure 14.

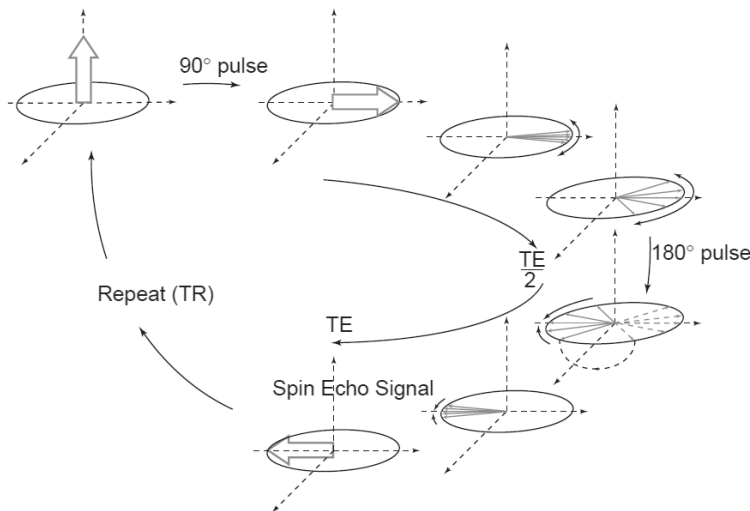


Figure 14 – Spin echo sequence [17].

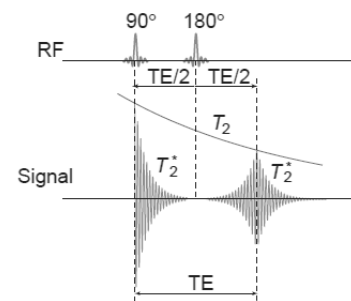


Figure 15 - Spin echo signal and exponential decay [17].

The maximal echo amplitude depends on T_2 and not in T_2^* since spin echo only affects dephasing caused by field inhomogeneities and has no effect on spin-spin interaction dephasing, Figure 15. Therefore, an exponential decay curve $M_0(e^{-TE/T_2})$ can be determined by multiple experiments at different echo times, and T_2 can be estimated [24].

Gradient Recalled Echo (GRE) sequence

In gradient recalled echo sequences, or simply gradient echo, the echo is produced by magnetic field gradients rather than pairs of RF pulses. This is done by first applying a frequency-encoding gradient with negative polarity to induce dephasing of precessing spins and then the gradient is reversed and the spins rephase forming a gradient echo (Figure 16).

Since gradient echoes do not need 180° refocusing pulse, very short repetition times (TR) can be achieved. The repetition time is determinant in overall scan time of most sequences which makes GRE sequence much faster than spin echo sequence [20]. Another advantage of GRE by not using a 180° pulse is that less total RF power is applied to the patient and thus less total RF energy is deposited within the tissue [15].

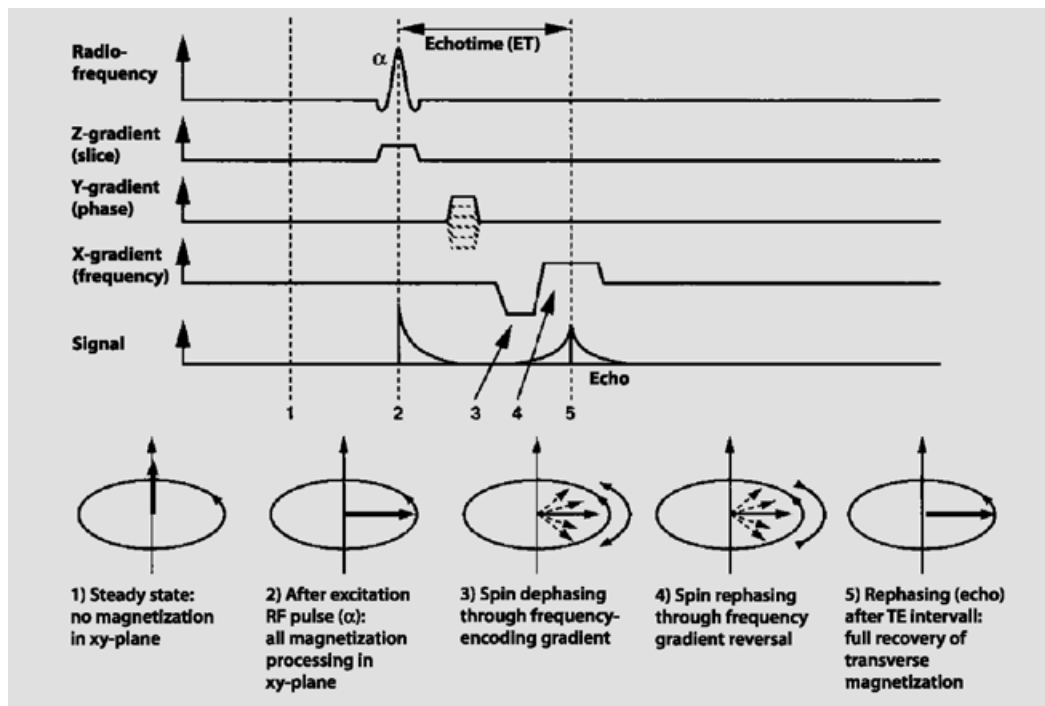


Figure 16 – Gradient echo sequence [20].

2.2. MRI at Ultrahigh Fields

A continuous increasing of MRI field strength can be observed alongside its development. More and more 3.0 T high field systems have been placed in clinical use beside 1.5 T conventional systems, and ultrahigh field (4 – 9.4 T) systems have been installed at a number of research sites for human studies [27]. One of the reasons for the rise of field strength is the increasing difference between spin up and spin down population with field strength. This leads to a higher signal, and thus, a higher signal-to-noise ratio (SNR) can be obtained [13]. A higher SNR can be traded for increasing spatial resolution or for decreasing imaging time [11].

Despite increased SNR at ultrahigh field (UHF) systems, several drawbacks are present. An increased B_0 inhomogeneities due to magnetic susceptibility differences between air and tissue [28] causes varying precession frequencies of the spins, which diminishes a homogeneous excitation and leads to a faster dephasing of the spins resulting in a shorter T_2^* [13]. However, B_0 inhomogeneities can be reduced by B_0 shimming.

The Larmor frequency of the RF field (B_1^+) applied, increases with the field strength, and higher the frequency shorter becomes the RF wavelength (Table 2). At 7.0 T, with frequencies near 300 MHz, the RF wavelength for protons in water is about 11cm, which leads regionally to negative interferences of superimposed RF waves. This creates inhomogeneities of the RF field in the body, which results in signal drop off in MR images, Figure 17 [13]. This constrain can be overcome by using surface array coils, by regulating the amplitude and the phase of each array channel [29].

| Field strength | Proton wavelength in air (cm) | Proton wavelength in water (cm) |
|-----------------------|--------------------------------------|--|
| 1.5 T | 470 | 52 |
| 3.0 T | 235 | 26 |
| 7.0 T | 100 | 11 |

Table 2 – RF wavelength in air and in water for proton at different field strengths [13].

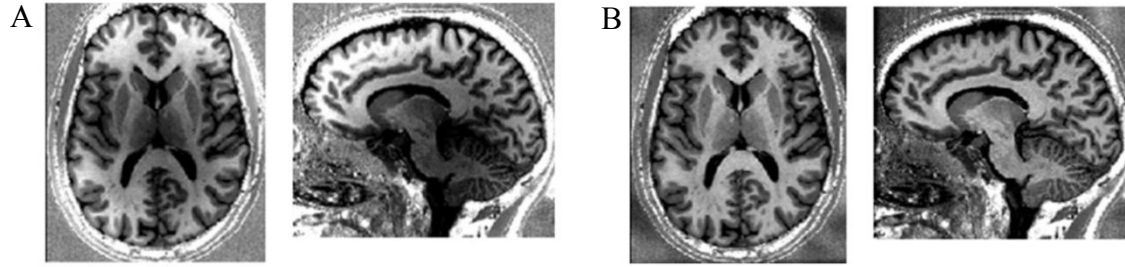


Figure 17 – A: Effects of RF field inhomogeneities on MRI. B: MRI with corrected RF field inhomogeneities. [30]

RF power deposition is another concern when referring to ultrahigh fields, as the RF field does not only affect the orientation of the net magnetization but also interacts with ions and molecules in the tissue [13]. The absorbed energy results in temperature rise that is higher for higher frequencies [13]. Thus, at UHF the risk of tissue heating and burning are increased. To avoid excessive tissue heating, regulatory organizations, such as Food and Drug Administration (FDA) and International Electrotechnical Commission (IEC), restricts the maximum input power of RF field in order to not exceed the specific absorption rate (SAR) limit (Table 3) [15,31]. The evaluation of SAR values is an important procedure at UHF MRI to assure patient safety [31].

| Limit | Whole-Body Average | Heat Average | Head, Trunk Local SAR | Extremities Local SAR |
|-------------------------------|---------------------------|---------------------|------------------------------|------------------------------|
| IEC (6-minute average) | | | | |
| Normal (all patients) | 2 W/kg (0.5°C) | 3.2 W/kg | 10 W/kg | 20 W/kg |
| First level (supervised) | 4 W/kg (1°C) | 3.2 W/kg | 10 W/kg | 20 W/kg |
| Second level (IRB approval) | 4 W/kg (>1°C) | >3.2 W/kg | >10 W/kg | >20 W/kg |
| Localized heating limit | 39°C in 10 g | 38°C in 10 g | | 40°C in 10 g |
| FDA | 4 W/kg for 15 min | 3 W/kg for 10 min | 8 W/kg in 1g for 10 min | 12 W/kg in 1g for 5 min |

Table 3 –International Electrotechnical Commission (IEC 60601-2-33:2010) and Food and US Drug Administration (FDA) guidelines on SAR and heating in human MRI studies. [32]

2.3. Fluorine (^{19}F) imaging

The feasibility of ^{19}F MRI was first demonstrated by Holland *et al.* [10] four years after the development of ^1H MRI. ^{19}F has 100% natural abundance, a spin of 1/2, and a gyromagnetic ratio of 40.08 MHz/T (see Table 1) and 83% of the sensitivity of ^1H .

The use of ^{19}F MRI also benefits from the similarity of gyromagnetic ratios of ^{19}F and ^1H (differs about 6%) which allows the use of the same equipment for both nuclei. The absence of ^{19}F background in biological tissue (trace amounts of ^{19}F present in teeth and bones are negligible) [10] makes this nuclei a good probe to assess the structure, function and molecular display of various diseases [12].

The ^{19}F MRI was usually performed at relatively low spatial (millimeters) and temporal (minutes to hours) resolution because of low concentration of ^{19}F atoms in region of interest, though, these limitations can be overcome by the increased SNR at higher field strength (e.g., 7T) and dedicated RF coils [12].

3. RADIOFREQUENCY (RF) COILS

As referred before, RF coils are used to excite the spins in order to produce a measurable transversal signal (in transmission (Tx) mode) and to receive this signal (in receive (Rx) mode). An RF coil can be characterized as transmit only, receive only or both transmit and receive (transceiver Tx/Rx) [33].

There are two types of RF coils, volume coil and surface coil. Volume coils surround either the whole body or a specific part of a body and are often carried out as birdcage coils. They consist of wires arranged like rungs of a birdcage along the z-axis of the scanner. Due to their predetermined structure, it is not possible to position the coil to an arbitrarily position on the patient and hence the typical applications of birdcage coils are the body coil, a head coil or extremity coils. These coils have the capability to generate a homogenous B_1^+ field over a large volume within the coil, however in higher magnetic fields the volume coils have some B_1^+ homogeneity constraints. [21]

Surface RF coils are RF coils placed directly on surface of the sample, which can be single or multiple turns of wire. This type of RF coil has an increased signal to noise ratio (SNR) due to its very close placement on the patient, and as it generally comprises a smaller imaging volume, less noise is present, since the major source of noise is usually the tissue. One drawback of this type of coils is its limited penetration depth, possible B_1^+ inhomogeneities and a reduced field-of-view (FOV) (the imaged area is more or less the size of the coil) [11,18].

A way to overcome reduced FOV is the application of a coil array, which consists of numerous single elements placed near each other. Therefore, the FOV can be increased and simultaneously benefits from the good SNR of surface coils [14]. Coil arrays can also be used to compensate for B_1^+ inhomogeneities by adapting the amplitude and phase of each transmitter independently to reduce the negative interferences of the RF waves [34]. These advantages made surface array coils preferred RF coils for UHF use, rather than volume coils.

The next sections describe general aspects of a surface coil.

3.1. RLC circuit

A simple loop surface coil can be described as a resonant RLC-circuit. This consists of inductance L, capacity C and resistance R representing the electrical losses, as illustrated in Figure 18. When connected to an alternating power source, the electrical energy is stored periodically within the magnetic field of the inductance or the electrical field of the capacitance. The resonant frequency of the RLC circuit is [14]

$$f = \frac{1}{2\pi\sqrt{LC}} \quad \text{Eq. 5}$$

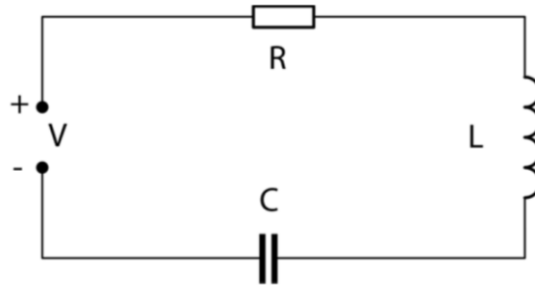


Figure 18 – An RLC resonant circuit in series [35].

When building RF surface coils for MRI, the inductance is determined by the geometry of the copper conductors. Therefore, the resonance frequency can only be changed by adjusting the value of the capacitors within the circuit. Inserting multiple capacitors has another purpose. As the wavelength at ultrahigh fields approaches the length of the conductors, there would be sites with no signal due to the zero phase of the sinusoidal wave. By inserting capacitors, they partition the RF coil, keeping the conductors short compared to the wavelength avoiding the zero phases. But each inserted capacitor increases the total loss within the RF coil and thus worsens the RF coils performance. By choosing a suitable number of capacitors, both effects can be balanced [36].

3.2. Tuning and Matching

The resonant circuit described previously needs to be tuned to the Larmor frequency of the protons in order to successfully excite them. Therefore, a tuning capacitor C_t is inserted in

the circuit. On the other hand the resonant circuit also needs to be matched to the impedance of the MR scanner and the coaxial cables, which is typically $50\ \Omega$, in order to achieve optimal signal transfer from the power source to the RF coil avoiding reflections that occur when the impedances differ. The matching can be handled by adding a matching capacitor C_m to the circuit. The Figure 19 shows an RLC circuit with additional tuning and matching capacitors [14].

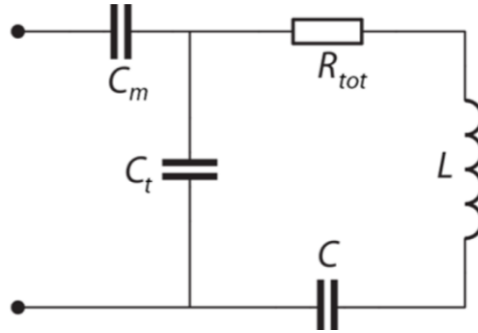


Figure 19 – Equivalent serial RLC circuit of an MRI coil with tuning-matching circuit [35].

3.3. Decoupling

When two loops are tuned to the same resonant frequency and placed near each other, their mutual inductance causes the resonances to split as shown in Figure 20. This results in a loss of sensitivity of the two coils. Therefore the neighboring elements have to be decoupled [34].

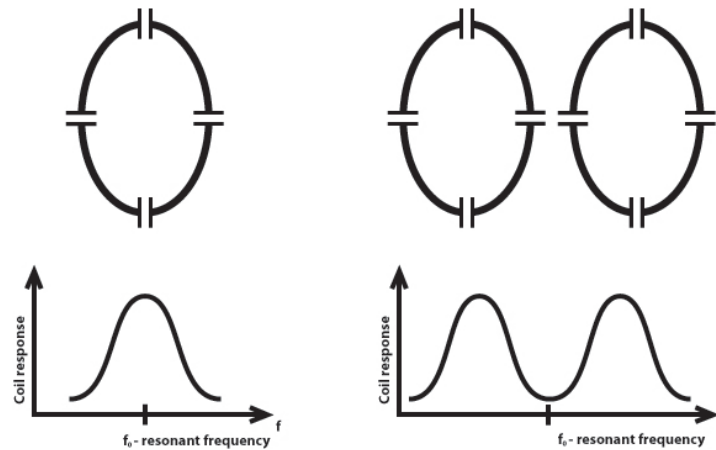


Figure 20 – Element coupling and frequency shift [34].

One of the decoupling methods is the overlap decoupling. It can be performed by moving two neighboring elements one upon the other so that they partially overlap. The magnetic flux, caused by one of the elements, is penetrating its neighboring element as well as the overlapping area, but in both cases with a different direction. Hence, their mutual inductance can be canceled out and the magnetic flux in the second element can be zeroed by adjusting the size of the overlap area. The drawbacks of this method are the geometrical constraints that go along with it. By partially overlapping two elements, the next-neighboring elements are automatically closer to each other and can therefore potentially couple stronger [37].

The Other way of how to decouple elements is the inductive or capacitive decoupling [38]. Two elements can be arranged so that they share a common conductor, illustrated in Figure 21, and an inductive or capacitive element can be brought into it. By adjusting the value of these elements, the mutual inductance of the elements can be cancelled out. As the losses of capacitive elements are usually lower, primarily capacitors are used for this purpose. One great advantage of this method is the possibility to decouple even non-adjacent element by connecting them with coaxial cables with two capacitors in between [37].

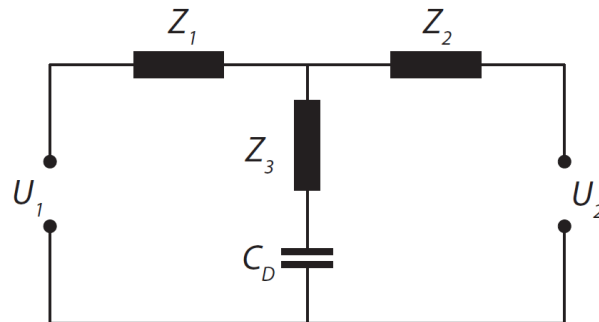


Figure 21 – Addition of a capacitor C_D between two elements that share a common conductor to avoid mutual inductance [35].

3.4. Cable Trap

Coaxial cables (Figure 22) are used to feed each element of the coil. On this type of cable, the current on the inner conductor and on the shield are equal and opposite so there is no energy to be radiated. However unbalanced current can be induced on the shield due to

unsymmetrical feeding of RF coil or from a near electromagnetic field, such as RF field. Under this situation, it can lead to increased power requirements, stronger coupling between the elements and cable heating in transmit mode, and also to significant decreased SNR in receive mode. A cable trap is a specialized circuit to suppress induced unbalanced current on the shield [34].

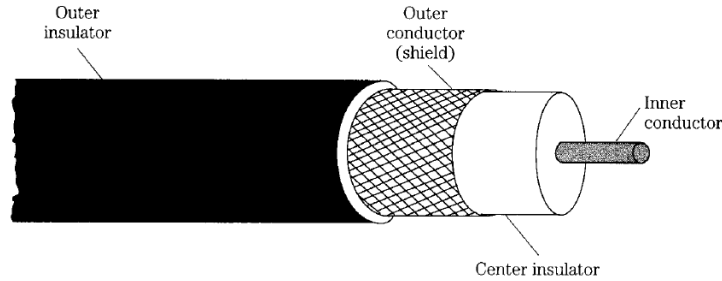


Figure 22 – Coaxial cable – cut away view [39].

3.5. Scattering-Parameters (S-Parameters)

The S-parameters describe the power transmission and reflection in a given system without knowledge about its components, and are therefore, used to quantify tuning, matching and decoupling. S-parameters are usually expressed in dB and organized in an S-parameter matrix. A network with N ports will have an N x N dimension S-matrix [40].



Figure 23 – A two-port component indicating the transmitted and reflected waves a_i and b_i [35].

Assuming a network with 2 ports, signals can be fed in (described by the parameter a_i) and read out (described by the parameter b_i) at 2 locations, as shown in Figure 23. The S-matrix will have the size of 2 x 2 and its entries are

$$S_{11} = \left. \frac{b_1}{a_1} \right|_{a_2=0} \quad \text{Eq. 6.1}$$

$$S_{21} = \left. \frac{b_2}{a_1} \right|_{a_2=0} \quad \text{Eq. 6.3}$$

$$S_{12} = \left. \frac{b_1}{a_2} \right|_{a_1=0} \quad \text{Eq. 6.2}$$

$$S_{22} = \left. \frac{b_2}{a_2} \right|_{a_1=0} \quad \text{Eq. 6.4}$$

S_{ii} is called the reflection coefficient, giving information about the fraction of the signal which is reflected at the port i and did not propagate through the component. On the other hand, the parameters S_{ij} , with $i \neq j$, represent the transmission coefficient, providing how much of the signal, inserted at port j , is transferred and lost into port i [40]. An example of a coil with two elements is shown on Figure 24.

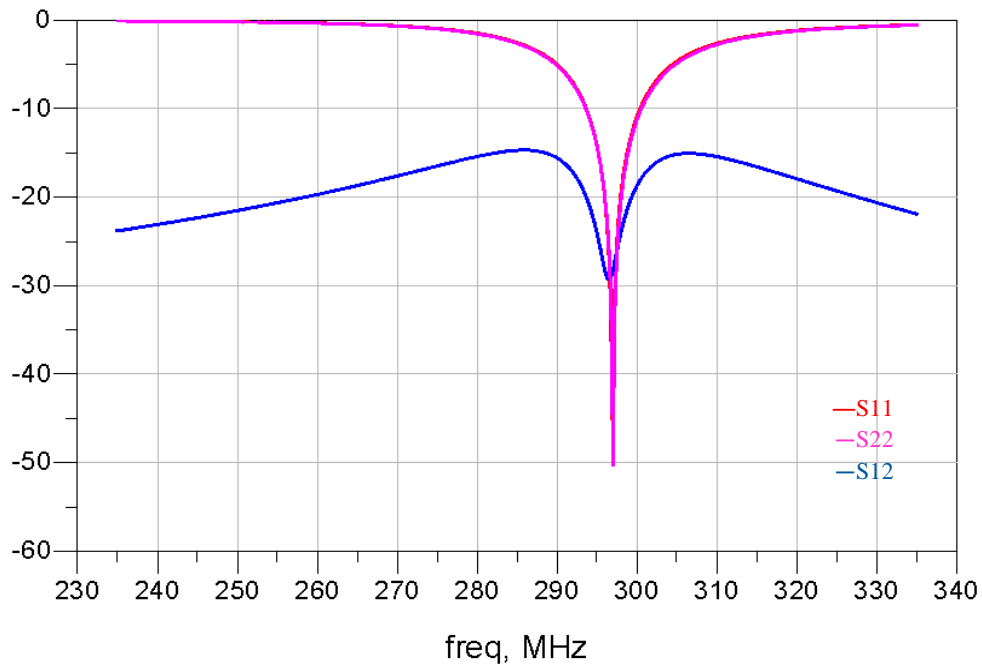


Figure 24 – S-parameters of a coil with 2 elements at 297 MHz. The reflection coefficient S_{11} and S_{22} are approximately -50 dB, which means only 0.00001 of the power transmitted is reflected back. The transmission coefficient S_{12} is -30 dB shows that 0.001 of the power inserted at element 1 is transmitted into element 2.

3.6. Quality factor

Quality factor or Q measures the performance of the coil (a tuned circuit) and is the ratio of stored energy to dissipated energy in the system. Equivalently, it can be seen as the ratio of the reactive impedance to the resistive impedance

$$Q = \frac{\omega L}{R} \quad \text{Eq. 7}$$

Quality factor is also a measure of the current or voltage magnification achieved by the coil. A higher Q means a narrower frequency response and the coil behaves like a band-pass filter, eliminating noise from outside the bandwidth of interest, and an improved SNR can be obtained [11].

The SNR is proportional to the square root of the loaded Q (Q_L – loaded to a sample such as a patient or a phantom) and an optimum SNR results when the sample noise is dominant, that is when the ratio of Q_L and unloaded Q (Q_{uL} – without any sample loaded) is less than 0.5 [19].

A practical way to calculate Q is using linear S_{11} curve of the coil tuned at f_0 and the bandwidth of Full Width at Half Maximum (FWHM) shown by Eq. 8 [41]

$$Q = \frac{f_0}{FWHM} \quad \text{Eq. 8}$$

4. MATERIALS AND METHODS

4.1 Coil Construction

In order to detect at 7.0 T both proton ($f = 297$ MHz) and fluorine ($f = 279.5$ MHz) signals a dual tunable transceiver array coil with eight elements was constructed. The coil was made of three parts, two identical anterior parts and one posterior part to fit the anatomy of an average knee, Figure 25.

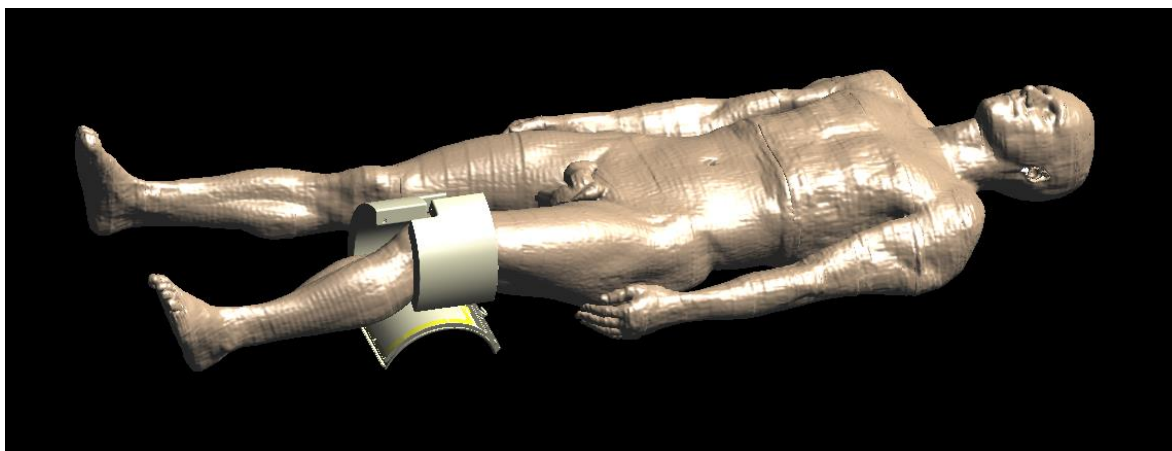


Figure 25 – $^1\text{H}/^{19}\text{F}$ dual tuned knee coil made of three parts: two identical anterior parts and one posterior part to fit the anatomy of an average knee.

Each of the anterior sections consists of three elements, each one with a size of 5×5 cm, were arranged in a triangular form in order to facilitate the decoupling of neighboring elements and bent to better cover the region of interest. As the short wavelength of RF field at 7.0 T leads to significant phase variations along the conductor, high Q ceramic capacitors were equally placed around the loop to shorten the conductor length. Decoupling between adjacent elements was allowed by a common conductor with a sharing decoupling capacitor with high Q. For tuning and matching trim capacitors (1-13 pF) with high Q were used. On right side of the Figure 26 trim and non-trim capacitor placements can be found.

Two of those elements placed above the knee were tuned to fluorine frequency and the lateral one to proton frequency, Figure 26 left.

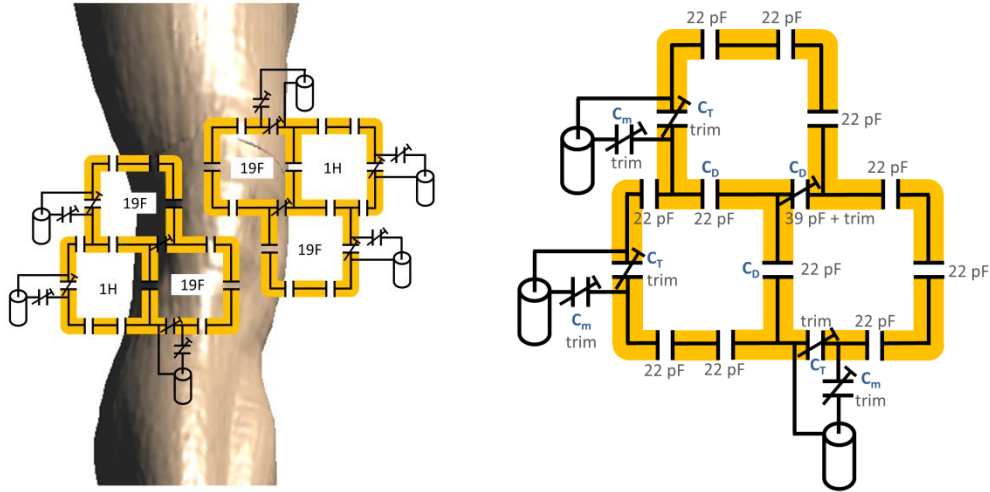


Figure 26 – Left: anterior part of the coil consisted by two identical 3 loop elements sections. Two of these loops, placed above the knee, were tuned to ^{19}F and the lateral one to proton frequency. Right: detail of one of the anterior section's circuit, where capacitors to shorten the conductor length and tuning, matching and decoupling capacitors are shown.

The posterior part of the coil consists of two elements with a size of 180×95 mm tuned to proton frequency. It was bended to fit the knee fold, serving as a comfortable support while measurements occur. Tuning, matching, decoupling capacitors and capacitors shortening the conductor length can be seen on Figure 27.

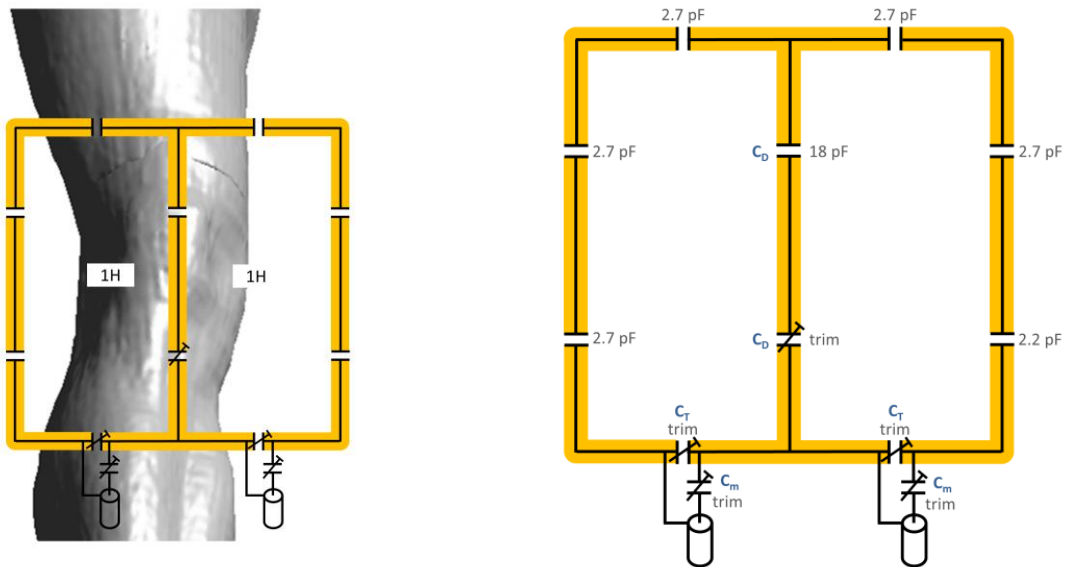


Figure 27 – Left: posterior part of the coil consisted by 2 loop elements tuned to proton frequency. Right: detail the posterior section's circuit, where capacitors to shorten the conductor length and tuning, matching and decoupling capacitors are shown.

The coils were manufactured from printed circuit board (PCB) using a computer numerical control (CNC) machine Promat S100 (LpKF, Garbsen, Germany). The width of the conductor was 10 mm to minimize ohmic losses.

4.1.1. Casing

A solid casing was designed to meet safety and comfort (Autodesk Inventor 2010, San Rafael, CA). It was built with the rapid prototyping system BST 1200es (Dimension, Eden Prairie, MN) using ABS (acrylonitrile butadiene styrene). The casing prevents a direct contact between the tissue and the coil, and thus avoiding tissue heating caused by high electric fields in the conductors and capacitors.

4.1.2. Cable trap

Cable traps were placed in the feeding coaxial cable of each element to suppress induced unbalanced current on the outer conductor at 279.5 MHz and 297.0 MHz for fluorine and proton cables, respectively. The cable trap was made out of two turns of the feeding cable with an adequate capacitor soldered to the outer conductor to adjust the frequency, Figure 28. The capacitor value was found using a pick-up loop.

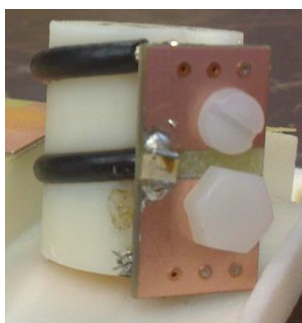


Figure 28 – Cable trap used in the coil. It consists of two turns of the feeding cable with a capacitor soldered to the shield.

4.2. Electromagnetic field (EMF) simulations

At B_0 higher than approximately 3.0 T, quasistatic solutions may no longer be employed, and the propagation of the magnetic field through the object has to be considered. The strength and phase of the RF field vary as function of position within the object, and determined by its form, permittivity, and conductivity. Even for simple geometrical configurations analytical solutions are difficult to obtain [42]. Hence, full wave simulation of the electromagnetic field is necessary to obtain complex behavior of RF field and RF power deposition in the tissues.

EMF simulations were carried out by the software SEMCAD X (Schmid & Partner Engineering AG, Zurich, Switzerland) based on finite-difference time-domain (FDTD) method that uses the differential form of Maxwell's equations for the discretization and computation of EM fields in a gridded 3D volume [43].

In order to find right capacitor values for capacitive shortening of the conductor and tuning, matching and decoupling of the elements, capacitors of the coil were modeled and simulated as $50\ \Omega$ ports. The resulting S-Parameters (saved as a touchstone file) were exported into an S-parameter simulator, Advanced Design System (ADS) (Agilent Technologies, Santa Clara, California, USA), where the optimal values were found. With these capacitors values, another EM simulation in SEMCAD X was carried out to obtain the correct electromagnetic field responses of the coil. Figure 29 shows SEMCAD X environment and Figure 30 and Figure 31 show ADS environment.

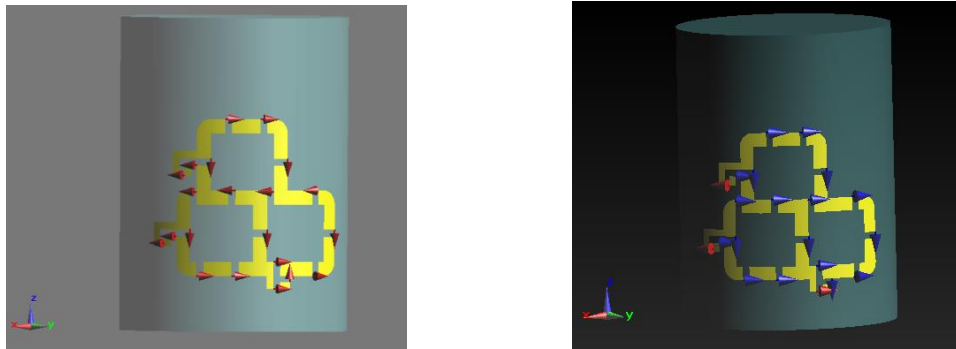


Figure 29 – Left: all capacitors were modeled and simulated as $50\ \Omega$ ports (in red) in order to be exported to ADS to be find optimal capacitive values. Right: the ports were replaced by capacitors (in blue) when their values were found on ADS.

4.2.1. Phantom simulation

EMF simulation of the coil was performed with the coil loaded to a phantom to access B_1^+ field patterns that would be compared to the measurements in order to validate the simulations (Figure 32 left). The phantom was modeled after a cylindrical phantom available at B.U.F.F. with similar tissue properties as an average knee ($\epsilon_r = 65$, $\sigma = 0.72$ S/m).

To balance accuracy and simulation time, the resolution of the mesh was set as 3 mm in all 3 dimensions over the phantom. Grid refinement was necessary to properly discretize the conductors and lumped elements (Figure 32 right) in order to produce realistic paths for the currents. The resulting grid had 3.06 million cells ($135 \times 154 \times 147$).

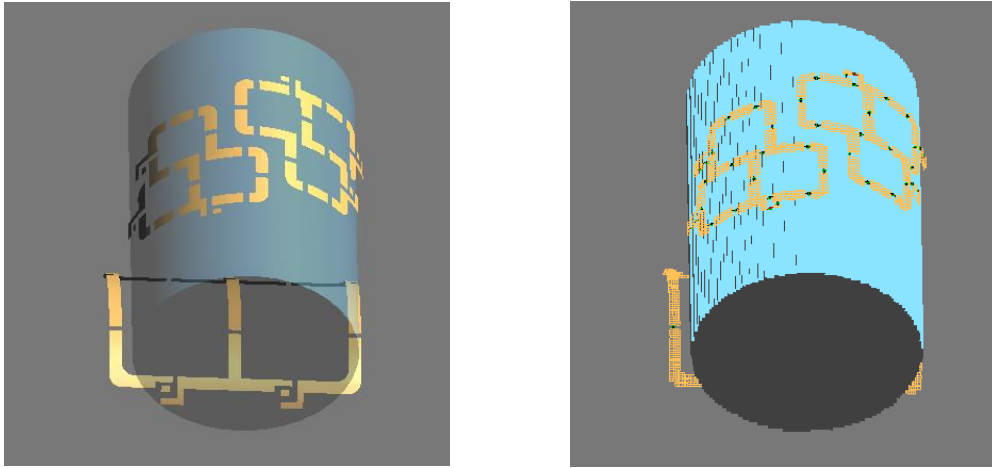


Figure 32 – Left: EM Simulation model of the phantom with the coil placed in a manner similar as in real-life measurements on the scanner. Right: Voxelized model.

4.2.2. Human model simulation

Human model simulations were performed with the posable human body model “Duke” (virtual family, IT’IS Foundation, Zurich, Switzerland). “Duke” model (male, age 34 years old, height 1.77 m, weight 72.4 kg) was developed from high resolution MRI scans of a healthy volunteer, and reconstructed as a 3D CAD object with approximately 80 high resolution organs and tissues [44].

To save simulation and post-processing time, only the lower part of the model was used, Figure 33. This was possible due to the local performance of surface coils.

The resolution of the mesh was set as 3 mm in all 3 dimensions over the region of interest. Grid refinement was conducted to proper discretization of the conductors and lumped elements. The resulting grid had 10.48 million cells ($232 \times 139 \times 325$).

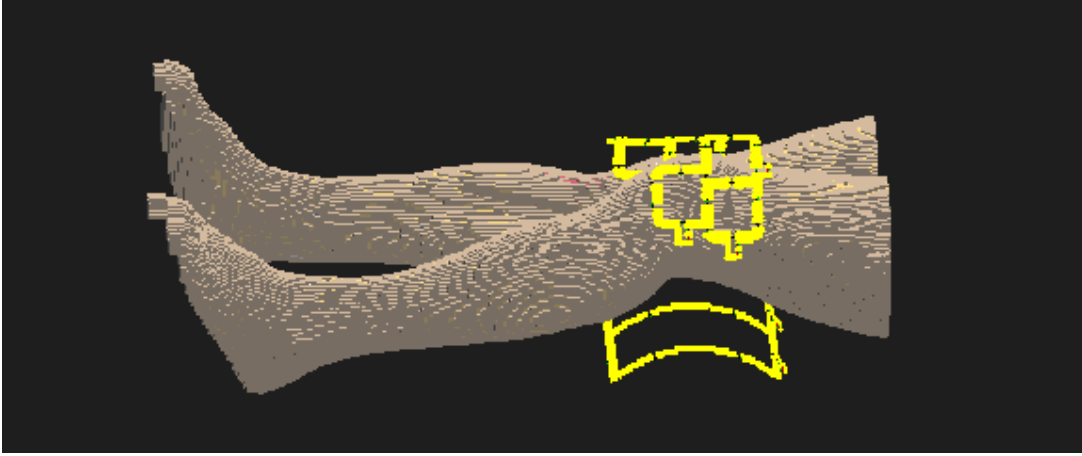


Figure 33 – Voxelized lower member of “Duke” with the coil.

SAR evaluation

Part of the energy carried by a time-harmonic EMF is deposited in lossy objects by induced conduction currents, which may result into local heating [43].

As mentioned before, SAR measures the energy absorbed by the biological tissues. The local SAR can be calculated with Eq. 9 when a specific location is given

$$SAR(\vec{r}) = \frac{\sigma}{2\rho} E^2 \quad \text{Eq. 9}$$

σ is the electrical conductivity, E^2 equals $\vec{E} \cdot \vec{E}^*$, the squared magnitude of the induced electric field, and ρ is the mass density. Local SAR is not always useful, as it is too sensitive to approximation in the computational methods. Therefore, averaged SAR in a region R with mass M is mostly used for safety concerns [43].

According to IEEE/IEC62704-1, R is recommended to be a cube aligned to the computational grid and sized to contain a specific M of lossy tissue (normally 1 g or 10 g).

The cube can also contain background material (air or other non-conductive tissues), however, it should not exceed more than 10% of the volume occupied by the cube. The cube is expanded at each location to compute the average SAR, resulting in a distribution of averaged SAR values along the entire region of interest.

The SAR evaluation was performed by post processing tool of SEMCAD X, MRI toolkit. This tool is able to combine magnetic and electric field of all or selected coil elements, and displays the result at selected frequencies.

The averaged SAR for the coil was calculated at 279.5 MHz and 297.0 MHz, by computing IEEE/IEC62704-1 constant mass cube of 10 g without any phase setting and with phase setting 3 (Table 15), which showed good B_1^+ homogeneity in the region of interest *in vivo*. The overall delivered power, which is the power delivered to all channel without losses, was set as 1 W, and equally distributed to each channel. The worst case SAR was also computed. The worst SAR is calculated by MRI toolkit of SEMCAD X by analyzing all possible phases and amplitudes for all active transmission ports, and then displays the setting that produces more SAR in the sample [43].

4.3. RF Bench analysis

For a circuit analysis of the coil an 8-channel vector network analyzer (VNA) ZVT8 (Rhode & Schwarz GmbH & Co. KG, Munich, Germany), with a frequency range of 3 kHz to 8 GHz, was used to assess the S-parameters.



Figure 34 – ZVT8 (Rhode & Schwarz GmbH & Co. KG, Munich, Germany).

4.3.1. Tuning, Matching and Decoupling

By connecting the coil directly to the VNA, the tuning, matching and decoupling of elements were possible by real-time assessment of the S-parameters.

4.3.2. Q factor measurement

The unloaded Q of each element of the coil was obtained using Eq. 8, with S-parameters acquired by VNA in unloaded conditions.

The loaded Q of each element was obtained with the coil loaded to a subject with 25 years old and 55 kg. It was also calculated with Eq. 8 using S-parameters obtained by the VNA.

4.4. Measurements

All images and spectroscopies were acquired on a 7.0 T whole-body scanner (Siemens Healthcare, Erlangen, Germany), Figure 35, equipped with an Avanto gradient system capable to achieve a slew rate of up to 200 mT/m/ms, maximum gradient strength of 40 mT/m (Siemens Medical Solutions, Erlangen, Germany) and an 8 kW RF amplifier (Stolberg HF-Technik, Stolberg-Vicht, Germany).



Figure 35 – 7.0 T whole-body scanner (Siemens Healthcare, Erlangen, Germany).

4.4.1. Coil interface

The connection between the coil and the scanner is carried out by the coil interface. It consists of a Tx/Rx switch box (Figure 36) with integrated low impedance preamplifiers, two 1 to 4 power splitter boxes (one for proton channels (Figure 37) and one for fluorine channels), and the coil plug with a coil file associated that bears the coil parameters, such as which nuclei is been scanned and RF power limitations. The power splitters were necessary since the power plug for the coil provided by the Siemens scanner consisted only in a single transmit plug.



Figure 36 – Tx/Rx switch box.

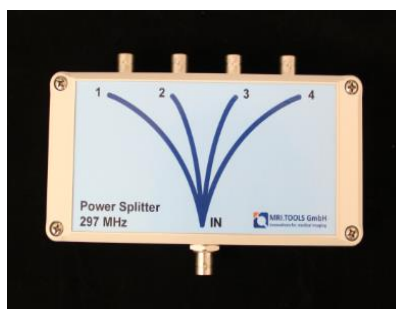


Figure 37 – 1 to 4 power splitter.

The coil interface described above, was used for the measurements of T_1 , T_2 , concentration curve and B_1^+ mapping measurements. Later, a specialized coil interface box (Figure 38) was constructed for $^1\text{H}/^{19}\text{F}$ dual tuned knee coil with integrated power splitters. This new coil interface was used for *in vivo* imaging and spectroscopy.



Figure 38 – Coil interface box specialized for $^1\text{H}/^{19}\text{F}$ dual tuned knee coil with integrated power splitters.

4.4.2. B_1^+ mapping

To validate the EMF simulations a comparison between simulated individual element and MR measured individual element B_1^+ maps were performed with a cylindrical phantom ($\epsilon_r = 65$, $\sigma = 0.72$ S/m) free of fluorine components.

The transmission field of each element was acquired with Bloch-Siegert implementation [45]. Each evaluated element was directly connected to the single power transmit plug of the scanner, while the remaining elements were connect to 50Ω power loads in order to absorb any power received through mutual coupling.

B_1^+ maps were done offline using Bloch simulations in Matlab (MathWorks Inc., Natick, Massachusetts, USA). The resulting maps were giving in arbitrary units (a. u.), hence, in order to allow the comparison between measured and simulated B_1^+ maps, a unit conversion to $\mu T/\sqrt{kW}$ was performed using Eq. 10.

$$B_1^+ [\mu T/\sqrt{kW}] = B_1^+ [a. u.] \frac{nominal B_1}{ReqVol} \sqrt{1000} \sqrt{50} \quad \text{Eq. 10}$$

The *nominal* B_1 is the achieved approximate flip angle and *ReqVol* is the required voltage, both given by Siemens scanner raw data. As the simulation does not have losses, the measurements were corrected to the hardware losses, Q-factors and S-parameters. The correction with S-parameters was necessary as the phantom did not contain fluorine, which made the maps for the fluorine channels be acquired at 1H frequency, therefore, the losses originated by not matched and tuned fluorine channels to 1H frequency could be corrected.

4.4.3. Determination of T_1 and T_2

^{19}F spectroscopy was performed in order to determine T_1 and T_2 of fluorine containing NSAID ointment (flufenamic acid (2- $\{[3-(\text{Trifluoromethyl}) \text{ phenyl}] \text{ amino}\}$ benzoic acid) used in this project. The measured samples were two cylindrical MR probes (inner diameter = 4.52 mm, height = 50 mm) filled with NSAID ointment, and 50% NSAID ointment plus

50% fluorine free ointment. In order to cover only one MR probe for each measurement, SPin ECho full Intensity Acquired Localized (SPECIAL) [46] technique was used (Figure 39). This technique allows data acquisition only in the ROI enclosed by a predefined voxel. For a more accurate position of the voxel, ^{19}F gradient-echo (GRE) images were acquired for orientation (TR = 90 ms, TE = 1.3 ms, in plane resolution: $2 \times 2 \text{ mm}^2$, slice thickness: 5 mm, matrix: 128×128).

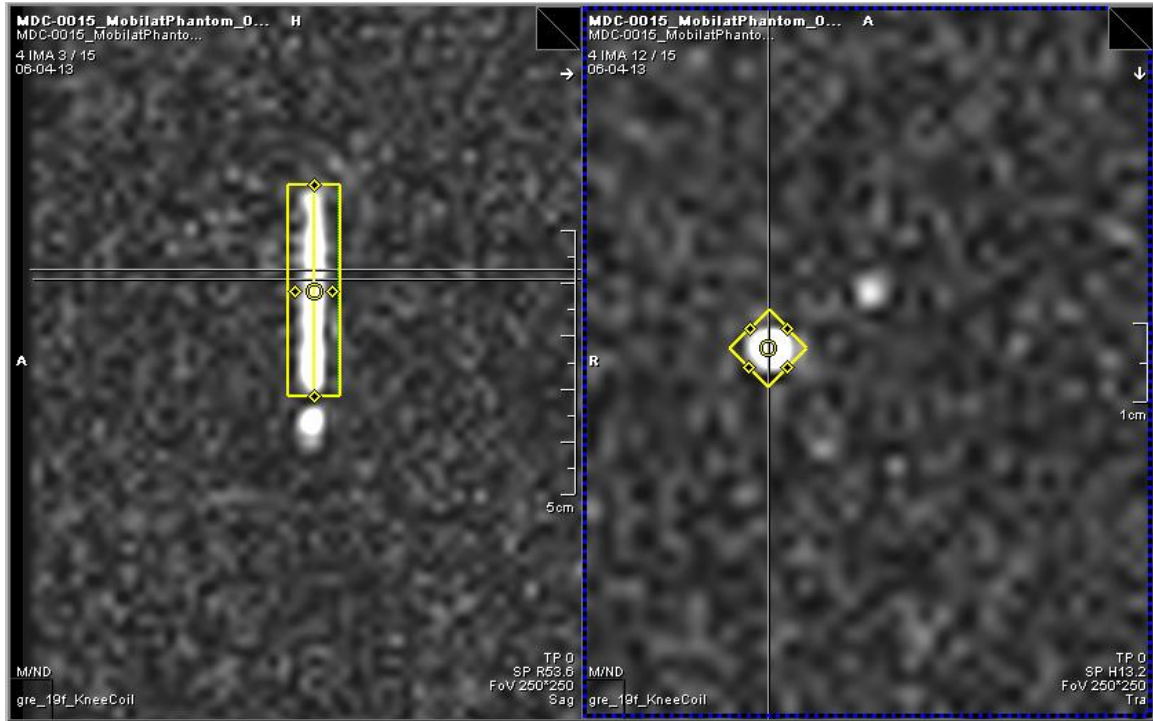


Figure 39 – ^{19}F GRE image (TR = 90 ms, TE = 1.3 ms, in plane resolution: $2 \times 2 \text{ mm}^2$, slice thickness: 5 mm, matrix: 128×128) of a sample filled with NSAID ointment. Left: sagittal view of SPECIAL voxel. Right: transversal view of SPECIAL voxel.

A voxel of size $7 \times 7 \times 40 \text{ mm}$ was placed around the MR probe. ^{19}F spectroscopy for T_1 measurements was performed with 128 averages, TE of 5.5 ms and different TR durations. ^{19}F spectroscopy for T_2 measurements were performed with 128 averages, TR of 4000 ms and different TE durations. The obtained data were processed in Matlab (MathWorks Inc., Natick, Massachusetts, USA) and fitted to T_1 and T_2 equations, described in section 2.1.5, in order to determine T_1 and T_2 relaxation times.

4.4.4. Calibration curve

For the calibration curve, which is the relationship between the amount of fluorine contained in the sample and the respect signal magnitude, spectroscopies were performed with TR of 2000 ms. TE of 5.5 ms, and different voxel sizes to limit different amount of the samples. The number of averages varies according to the voxel size to assure the same SNR for all measurements.

4.4.5. *In vivo* Imaging

High resolution GRE proton images (TR = 12 ms, TE = 3.4 ms, in plane resolution: $0.7 \times 0.7 \text{ mm}^2$, slice thickness: 5 mm, matrix: 384×384) and fluorine images (TR = 90 ms, TE = 1.3 ms, in plane resolution: $2 \times 2 \text{ mm}^2$, slice thickness: 5 mm, matrix: 128×128) were acquired.

In vivo B_1^+ shimming was performed using different phase settings to obtain a more homogeneous B_1^+ distribution over the region of interest.

4.4.6. *In vivo* ^{19}F Spectroscopy

As there were no volunteers with active inflammation on the knee available at moment of this study, two healthy subjects were asked to apply topically the flufenamic acid containing NSAID ointment on the skin surrounding the knee, in order to detect eventual ointment absorption. For this purpose unlocalized ^{19}F spectroscopy using FID was regularly performed, and any change of initial signal magnitude can be used to trace substance absorption.

Subject 1 applied topically 5.82 g of the NSAID ointment, corresponding to 0.621 mmol of flufenamic acid, and was monitored approximately 70 minutes without leaving the scanner.

Subject 2 was asked to apply 9.65 g of the NSAID ointment, containing 1.03 mmol of flufenamic acid, and was monitored 172 minutes in two scan sessions, with each one not exceeding 50 minutes. At end of the session, after 172 minutes of the first spectroscopy, a

SPECIAL voxel spectroscopy was performed. The voxel was placed inside the knee under NSAID ointment application as shown in Figure 40.

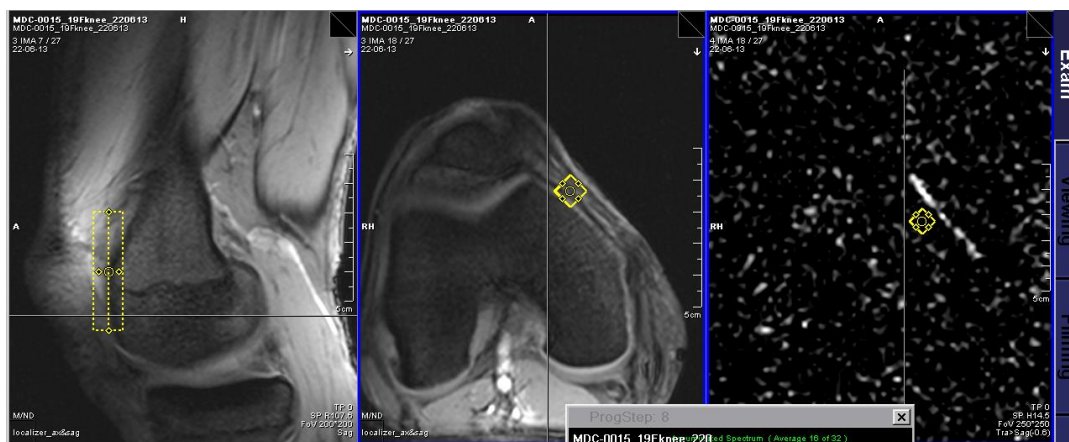


Figure 40 – SPECIAL voxel placement inside the knee under NSAID ointment application. Left: sagittal view of GRE ^1H image (TR = 12 ms, TE = 3.4 ms, in plane resolution: $0.7 \times 0.7 \text{ mm}^2$, slice thickness: 5 mm, matrix: 384×384). Center: axial view of GRE ^1H image (TR = 12 ms, TE = 3.4 ms, in plane resolution: $0.7 \times 0.7 \text{ mm}^2$, slice thickness: 5 mm, matrix: 384×384). Right: axial view of ^{19}F GRE image (TR = 90 ms, TE = 1.3 ms, in plane resolution: $2 \times 2 \text{ mm}^2$, slice thickness: 5 mm, matrix: 128×128).

5. RESULTS

To facilitate description of the results, the coil elements were numbered in Figure 41.

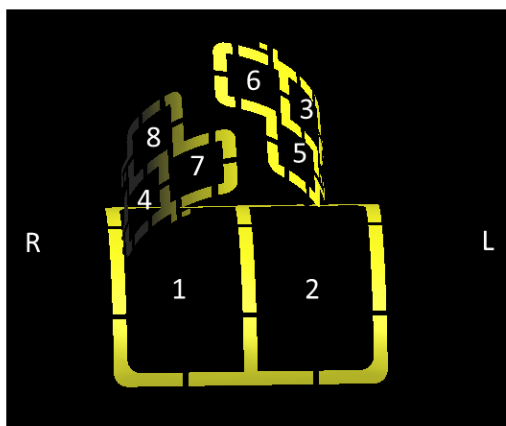


Figure 41 – Elements numbering. Channels 1-4 are ^1H channels and 5-8 are ^{19}F channels.

5.1. Coil Layout

The constructed coil is shown in figures below. On Figure 42, the coil PCB circuits, soldered capacitors and cable traps for each channel can be observed. Figure 43 shows how the coil in its casing is placed on a volunteer.



Figure 42 – PCB circuit and capacitors of the coil. Cable traps for each channel can be also observed.



Figure 43 – placement of the coil in its casing on a volunteer.

5.1.1. Cable traps

The performance of the cable traps associated to each channel as well as the capacitor value used are described in Table 4.

| Associated channel | Capacitor value | S_{11} |
|--------------------|-----------------|----------|
| 1 | 4.7 | -13 |
| 2 | 4.3 | -20 |
| 3 | 3.9 | -18 |
| 4 | 4.3 | -20 |
| 5 | 4.7 | -14 |
| 6 | 5.4 | -13 |
| 7 | 4.5 | -20 |
| 8 | 4.7 | -16 |

Table 4 – capacitors used for cable traps of associated channels and their performance.

5.2. RF Bench Analysis

5.2.1. S-Parameters

Each of coil elements were tuned to their respective 279.5 MHz (^{19}F frequency) or 297.0 MHz (^1H frequency) loaded on the knee of a subject (female, 1.63 m, 55 kg).

Reflection and transmission coefficients of each of three parts of the coil are presented in table below. Respective S-parameters visualizations on VNA can be found on Figure 44 to Figure 46.

| Coil part | Sii | 279.5 MHz | 297.0 MHz | Sij | 279.5 MHz | 297.0 MHz |
|---------------------|-----|-----------|-----------|-----|-----------|-----------|
| Posterior part | S11 | - | -32 dB | S12 | - | |
| | S22 | - | -35 dB | | | |
| Left anterior part | S66 | -39 dB | - | S63 | -20 dB | -19 dB |
| | S33 | - | -39 dB | S35 | -17 dB | -16 dB |
| | S55 | -34 dB | - | S65 | -25 dB | - |
| Right anterior part | S77 | -46 dB | - | S74 | -19 dB | -18 dB |
| | S44 | - | -39 dB | S48 | -19 dB | -19 dB |
| | S88 | -50 dB | - | S78 | -20 dB | - |

Table 5 – Sii and Sij of coil elements. Note that the S-parameter acquirement was made for each coil part.

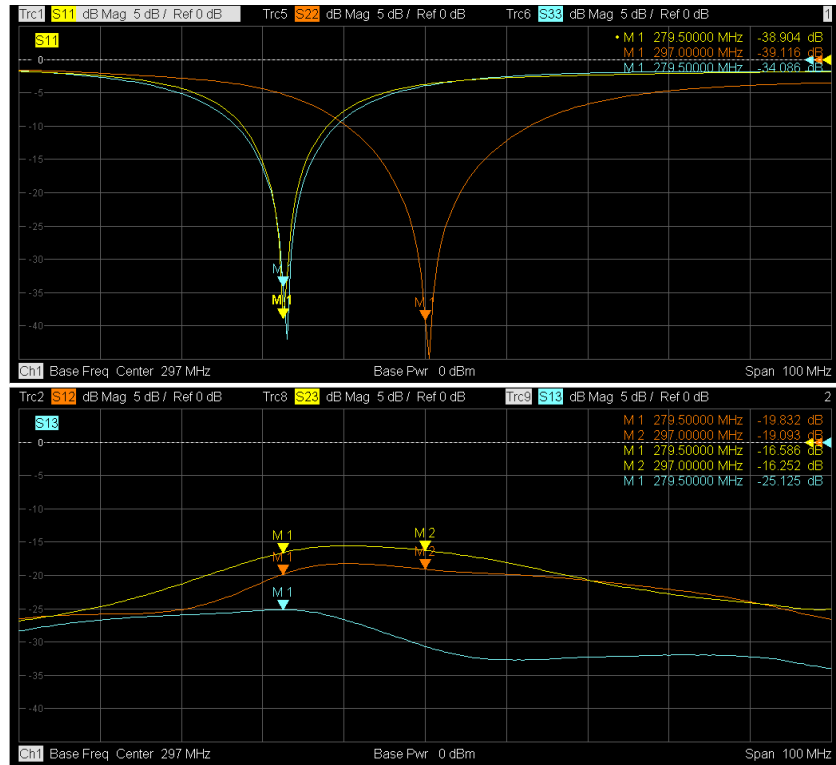


Figure 44 – print of VNA screen while measuring S-parameters for left anterior part of the coil.

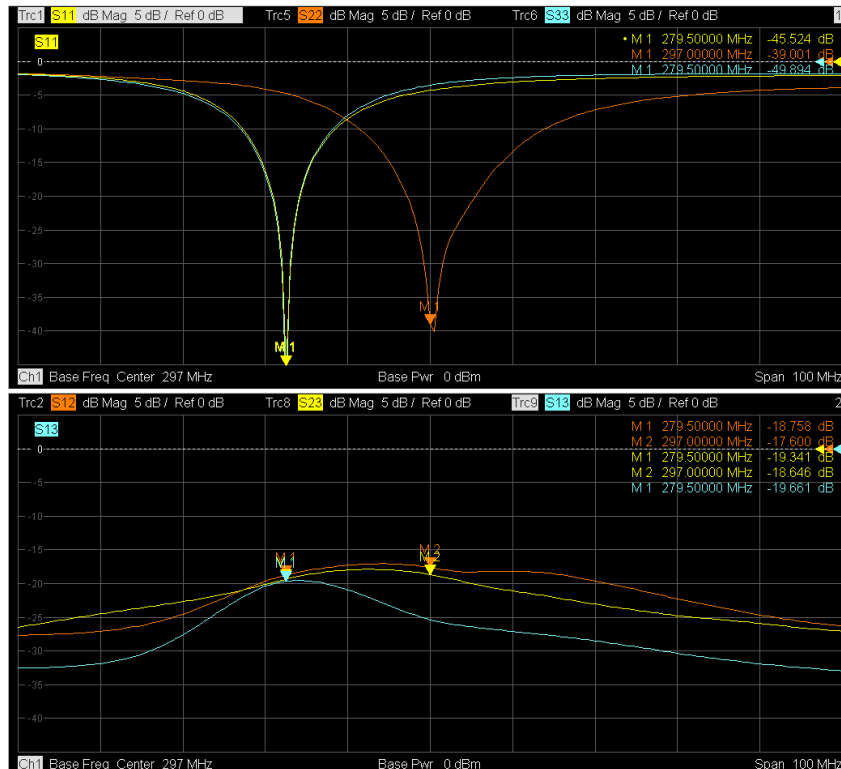


Figure 45 - print of VNA screen while measuring S-parameters for right anterior part of the coil.



Figure 46 - print of VNA screen while measuring S-parameters for the posterior part of the coil.

5.2.2. Q-factor

Loaded and unloaded Q as well as the ratio of loaded Q to unloaded Q is presented in the table below.

| channels | Q_L | Q_{uL} | Q_L/Q_{uL} |
|----------|-------|----------|--------------|
| 1 | 6.5 | 29.7 | 0.22 |
| 2 | 8.9 | 18.6 | 0.48 |
| 3 | 7.7 | 31.3 | 0.25 |
| 4 | 7.7 | 49.5 | 0.16 |
| 5 | 12.7 | 46.6 | 0.27 |
| 6 | 14.7 | 111.8 | 0.13 |
| 7 | 13.6 | 124.2 | 0.11 |
| 8 | 13.6 | 62.1 | 0.22 |

Table 6 – Q_L , Q_{uL} and Q_L/Q_{uL} of each coil channels.

5.3. Simulated and measured B_1^+ maps

The measured B_1^+ maps corrected to hardware losses (from the Tx/Rx switch box, scanner power transmit plug and feeding cables), to Q-factors and to S-parameters are shown in Table 7.

Simulated and measured B_1^+ maps are compared on Table 8 and displayed in Figure 47 together with the maximum B_1^+ value of each channel. The B_1^+ maps are shown by their relative values to simulated and measured maximum values, respectively.

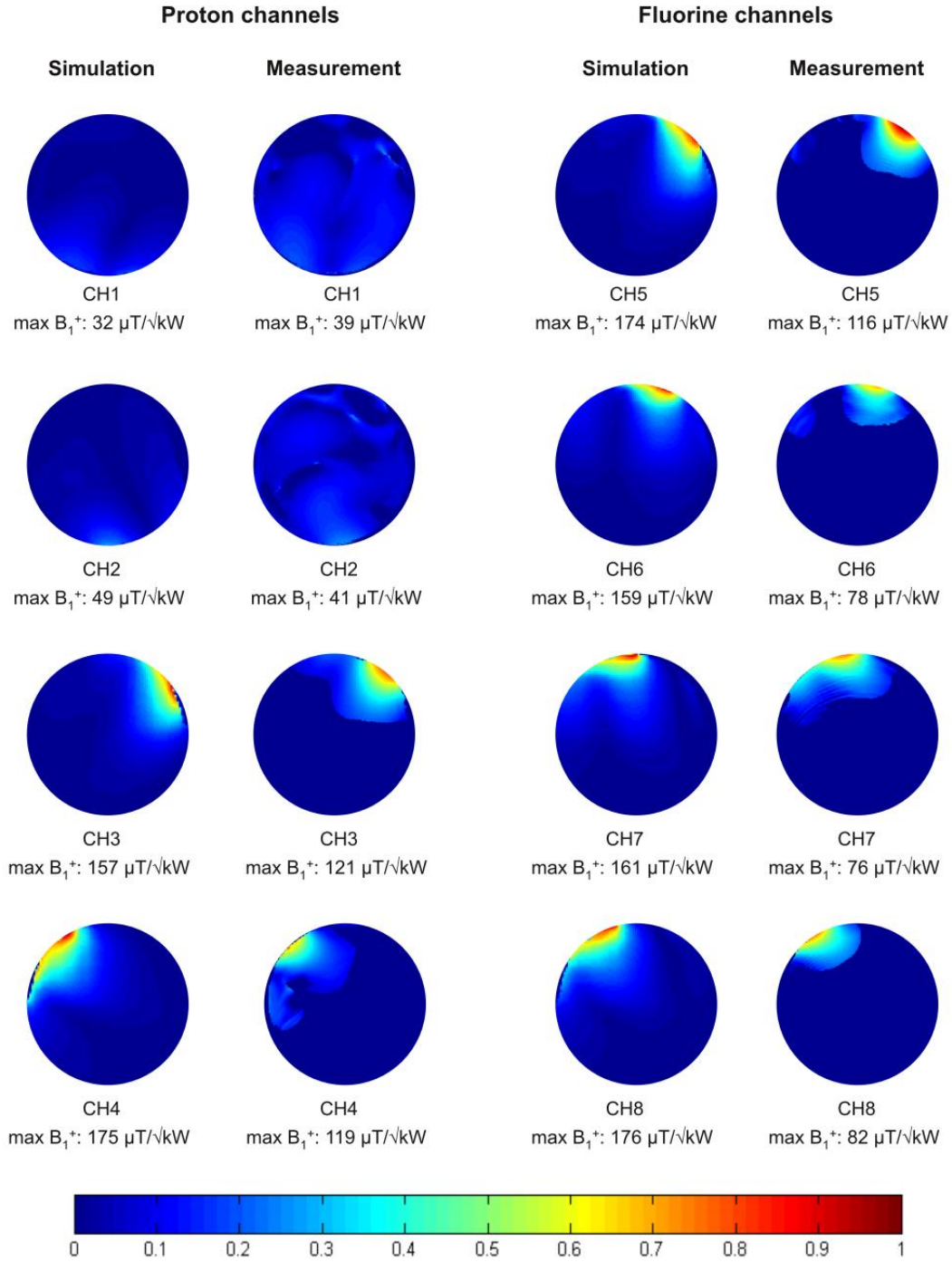


Figure 47 – Relative B_1^+ map of simulation and measurement. The maximum B_1^+ value of each channel is shown below its map.

| channel | Hardware losses (linear) | Q_L/Q_{uL} | S_{ii} (linear) | Measured B_1^+ (a.u.) | Measured B_1^+ ($\mu T/\sqrt{kW}$) | Measured B_1^+ corrected with hardware loss ($\mu T/\sqrt{kW}$) | Measured B_1^+ corrected with hard. Loss + Q ($\mu T/\sqrt{kW}$) | Measured B_1^+ correc. with hard. Loss + Q + S-param ($\mu T/\sqrt{kW}$) |
|---------|--------------------------|--------------|-------------------|-------------------------|--|---|--|--|
| 1 | 0.54 | 0.22 | - | 0.9619 | 25.25823 | 34.27617579 | 38.74828847 | 38.74828847 |
| 2 | 0.54 | 0.48 | - | 0.8299 | 21.79208 | 29.79315268 | 41.23286951 | 41.23286951 |
| 3 | 0.55 | 0.25 | 0.000622 | 2.9868 | 78.42944 | 105.6703619 | 121.7556467 | 121.7935426 |
| 4 | 0.56 | 0.16 | 0.001709 | 3.1213 | 81.96123 | 109.6794355 | 119.3690178 | 119.4711279 |
| 5 | 0.55 | 0.27 | 0.440018 | 2.0864 | 54.78612 | 73.81883746 | 86.55561424 | 115.6666174 |
| 6 | 0.54 | 0.13 | 0.3926 | 1.5818 | 41.53599 | 56.46822568 | 60.59513996 | 77.74998318 |
| 7 | 0.55 | 0.11 | 0.402949 | 1.5564 | 40.86902 | 55.24755848 | 58.55323896 | 75.77835632 |
| 8 | 0.56 | 0.22 | 0.416045 | 1.5732 | 41.31016 | 55.28071251 | 62.57099931 | 81.88102884 |

Table 7 – Correction factors of measured B_1^+ maps – hardware losses, Q_L/Q_{uL} and S_{ii} , the obtained measured B_1^+ maps (a. u.) and after correction factors. S_{ii} of channels 1 and 2 was not registered before B_1^+ mapping experiment, but as they are proton channels and they were well tuned and matched to proton frequency, hence, the S-parameter correction of these channels would be negligible.

| channel | Simulated B_1^+ ($\mu\text{T}/\sqrt{\text{kW}}$) | Measured B_1^+ ($\mu\text{T}/\sqrt{\text{kW}}$) | Simulated B_1^+ – Measured B_1^+ ($\mu\text{T}/\sqrt{\text{kW}}$) | $\frac{\text{measured}}{\text{simulated}}$ | $1 - \frac{\text{measured}}{\text{simulated}}$ |
|---------|---|--|---|--|--|
| 1 | 32.4 | 38.7 | -6.3 | 1.20 | -0.20 |
| 2 | 49 | 41.2 | 7.8 | 0.84 | 0.15 |
| 3 | 157 | 121.8 | 35.2 | 0.78 | 0.22 |
| 4 | 175 | 119.5 | 55.5 | 0.68 | 0.32 |
| 5 | 174 | 115.7 | 58.3 | 0.66 | 0.34 |
| 6 | 159 | 77.7 | 81.3 | 0.49 | 0.51 |
| 7 | 161 | 75.8 | 85.2 | 0.47 | 0.53 |
| 8 | 176 | 81.9 | 94.1 | 0.47 | 0.53 |

Table 8 – Simulated and measured B_1^+ values and their comparison.

5.4. SAR evaluation

Peak averaged SAR at 279.5 MHz and 297.0 MHz, computed with IEEE/IEC62704-1 constant mass cube of 10 g with total input power of 1 W for no phase setting and for phase setting 3 is shown in Table 9, as well as worst the case SAR. This worst case scenario is calculated by MRI toolkit of SEMCAD X for all possible phase settings and amplitudes of the transmission power in each port, with 1 W as total input power. The resulting phases and amplitudes of worst case SAR are shown in Table 10.

SAR distribution over the region of interest is shown for phase setting 3 at 279.5 MHz in Figure 48 and at 279.0 MHz in Figure 49.

| | no phase settings (1 W input power) | phase setting 3 (1 W input power) | Worst case SAR (1 W input power) |
|-------------------------------------|--|--------------------------------------|-------------------------------------|
| Peak 10 g averaged SAR at 279.5 MHz | 0.495 W/kg | 0.306 W/kg | 3.033 W/kg |
| Peak 10 g averaged SAR at 297.0 MHz | 0.475 W/kg | 0.375 W/kg | 1.769 W/kg |

Table 9 - Peak averaged SAR at 279.5 MHz and 297.0 MHz computed with IEEE/IEC62704-1 constant mass cube of 10 g for no phase setting, for phase setting 3 and worst case SAR.

| Worst case SAR (for 1 W input power) | | | | |
|--------------------------------------|-----------|-----------|-----------|-----------|
| Channel | 279.5 MHz | | 297.0 MHz | |
| | Phase | Amplitude | Phase | Amplitude |
| 1 | 105.12° | 0.0007 W | 79.75° | 0.1052 W |
| 2 | 55.35° | 0.0003 W | 118.25° | 0.1123 W |
| 3 | 122.70° | 0.0016 W | -157.36° | 0.7661 W |
| 4 | -10.02° | 0.0233 W | -153.97° | 0.0041 W |
| 5 | -128.24° | 0.0142 W | 157.17 | 0.0045 W |
| 6 | 42.81° | 0.0221 W | 91.01° | 0.0070 W |
| 7 | -180.00° | 0.5069 W | -180.00° | 0.0002 W |
| 8 | -1.15° | 0.4309 W | 122.53° | 0.0005 W |

Table 10 – The phase and amplitude of worst case SAR at ^{19}F and ^1H frequencies.

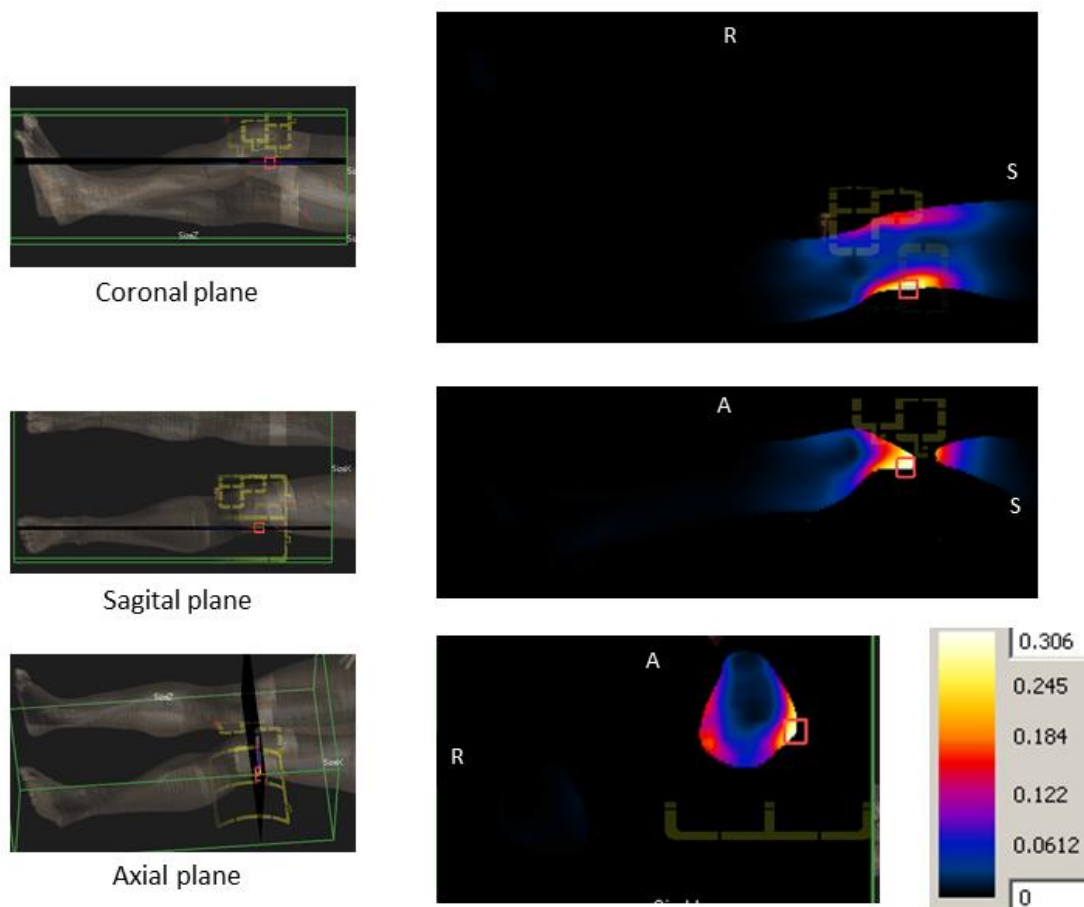


Figure 48 – 10 g averaged SAR distribution at 279.5 MHz for phase setting 3.

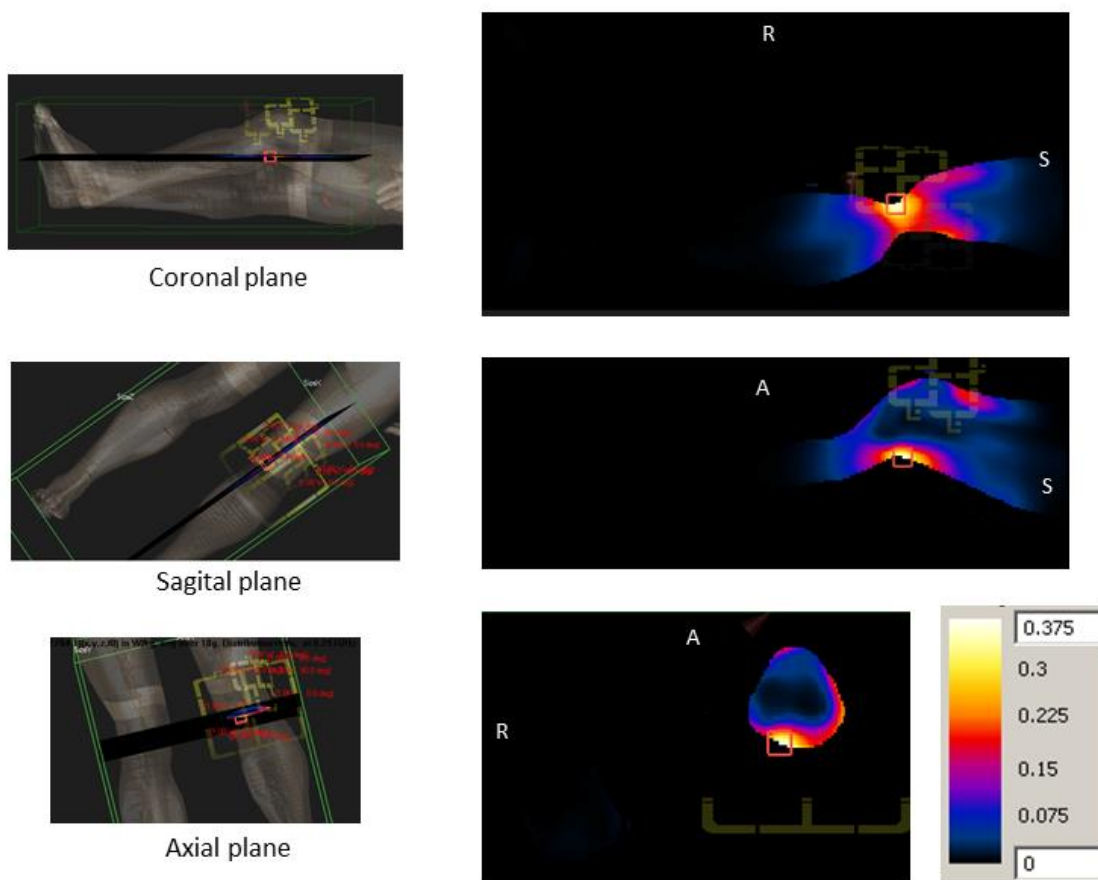


Figure 49 - 10 g averaged SAR distribution at 297.0 MHz for phase setting 3.

5.5. T_1 measurement

Signal magnitude of FID of different samples at different TRs was registered in Table 11. The acquired data was plotted and fitted to the T_1 equation, shown in Figure 50. T_1 was found as 673 ms for 100% NSAID ointment and 616 ms for 50% NSAID ointment + 50% fluorine free ointment.

| TR (ms) | Signal magnitude a.u. ($\times 10^{-6}$) 100% NSAID ointment (65 μmol of flufenamic acid) | Signal magnitude a.u. ($\times 10^{-6}$) 50% NSAID ointment + 50% fluorine free ointment (32 μmol of flufenamic acid) |
|---------|--|---|
| 260 | 3.650414713 | 1.857248084 |
| 500 | 6.619002951 | 3.623145289 |
| 750 | 8.555848297 | 4.43542712 |
| 1000 | 9.585644839 | 5.140411854 |
| 1250 | 10.71735259 | 5.371996585 |
| 1500 | 11.21005678 | 5.659231852 |
| 1750 | 11.37189668 | 5.757178825 |
| 2000 | 11.90929343 | 6.118101368 |
| 3000 | 12.34120536 | 6.136087312 |
| 4000 | 12.42318758 | 6.189797488 |
| 5000 | 12.47302942 | 6.307514114 |

Table 11 - Signal magnitude of spectroscopies of 100% NSAID ointment sample and 50% NSAID ointment + 50% fluorine free ointment sample at different TRs.

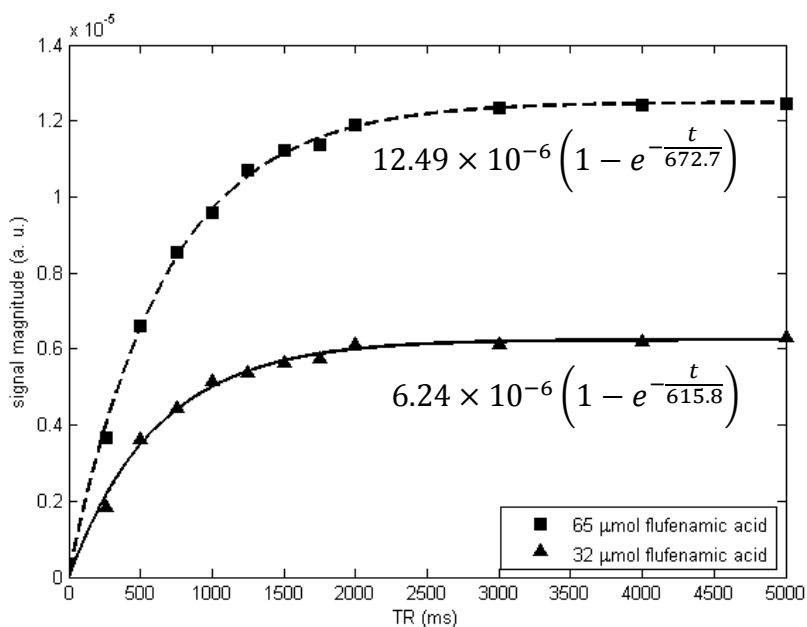


Figure 50 – Fitted T_1 recovery curve from acquired data.

5.6. T₂ measurement

Signal magnitude of FID for the different samples at different TEs was registered in Table 12. The acquired data was plotted and fitted to the T₂ equation shown in Figure 51. T₂ was found as 31.07 ms for 100% NSAID ointment and 25.87 ms for 50% NSAID ointment + 50% fluorine free ointment.

| TE (ms) | Signal magnitude a.u. ($\times 10^{-6}$) 100% NSAID ointment (65 μ mol of flufenamic acid) | Signal magnitude a.u. ($\times 10^{-6}$) 50% NSAID ointment + 50% fluorine free ointment (32 μ mol of flufenamic acid) |
|---------|--|---|
| 5.5 | 12.49374738 | 6.82736343 |
| 8 | 11.89928515 | |
| 9 | | 5.41190389 |
| 10 | 11.21772892 | |
| 12 | 10.47904098 | |
| 15 | 9.295233851 | 3.947644809 |
| 20 | | 3.444100231 |
| 30 | 5.833485836 | 2.429228108 |
| 40 | 4.098662036 | 1.790736375 |
| 50 | | 1.562887196 |
| 60 | 2.287997288 | 0.737952665 |
| 70 | | |
| 80 | 0.995964142 | |
| 100 | 0.611352291 | |
| 120 | 0.436143606 | |

Table 12 - Signal magnitude of spectroscopies of 100% NSAID ointment sample and 50% NSAID ointment + 50% fluorine free ointment sample at different TEs.

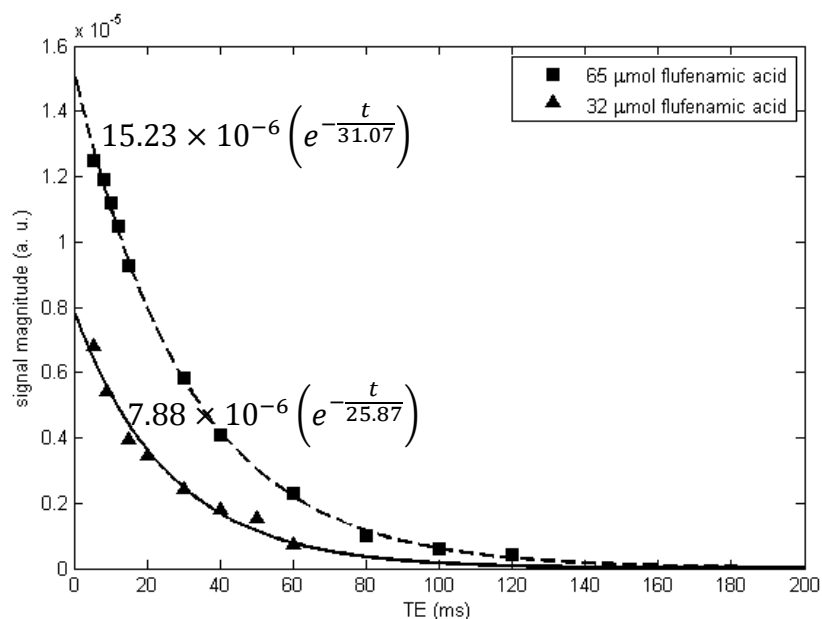


Figure 51 – Fitted T_2 recovery curve from acquired data.

5.7. Calibration Curve

Signal magnitude of the spectroscopy and amount of flufenamic acid present at different SPECIAL voxel sizes for 100% NSAID ointment can be found in Table 13 and, for 50% NSAID ointment + 50% fluorine free ointment is registered in Table 14. The concentration curves are plotted in Figure 52.

| Voxel size (mm ³) | Amount of Fluf. Acid (μmol) | Signal magnitude a.u. (×10 ⁻⁶) |
|-------------------------------|-----------------------------|--|
| 7 x 7 x 30 | 51.1 | 10.84 |
| 7 x 7 x 27 | 46.0 | 10.12 |
| 7 x 7 x 24 | 40.8 | 9.44 |
| 7 x 7 x 21 | 35.7 | 8.30 |
| 7 x 7 x 18 | 30.6 | 7.19 |
| 7 x 7 x 15 | 25.5 | 6.09 |
| 7 x 7 x 12 | 20.4 | 4.91 |
| 7 x 7 x 9 | 15.3 | 3.84 |

Table 13 - Signal magnitude of spectroscopies and amount of flufenamic acid present at different SPECIAL voxel sizes for 100% NSAID ointment sample.

| voxel size (mm ³) | Amount of Fluf. Acid (μmol) | Signal magnitude a.u. (×10 ⁻⁶) |
|-------------------------------|-----------------------------|--|
| 7 x 7 x 30 | 25.5 | 6.42 |
| 7 x 7 x 27 | 23.0 | 5.64 |
| 7 x 7 x 24 | 20.4 | 5.02 |
| 7 x 7 x 21 | 17.9 | 4.43 |
| 7 x 7 x 18 | 15.3 | 3.92 |
| 7 x 7 x 15 | 12.8 | 3.10 |
| 7 x 7 x 12 | 10.2 | 2.61 |
| 7 x 7 x 9 | 7.7 | 1.86 |

Table 14 - Signal magnitude of spectroscopies and amount of flufenamic acid present at different SPECIAL voxel sizes for 50% NSAID ointment + 50% fluorine free ointment sample.

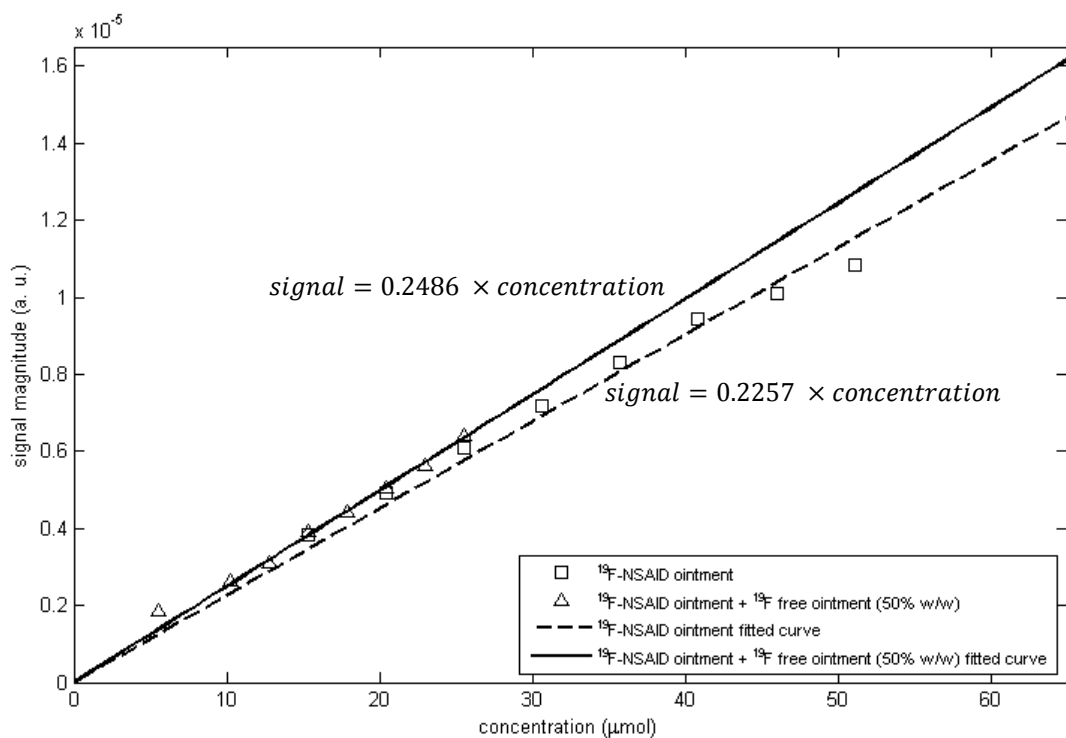


Figure 52 – Concentration curves for 100% NSAID ointment and for 50% NSAID ointment + 50% fluorine free ointment.

5.8. *In vivo* Imaging

5.8.1. B_1^+ Shimming

| | | |
|--|--|---|
| Phase setting 1 Ch1: 0° Ch2: 180° Ch3: 90° Ch4: 0° Ch5: 180° Ch6: 0° Ch7: 90° Ch8: 0° | Phase setting 2 Ch1: 0° Ch2: 180° Ch3: 0° Ch4: 90° Ch5: 0° Ch6: 180° Ch7: 90° Ch8: 0° | Phase setting 3 Ch1: 0° Ch2: 90° Ch3: 0° Ch4: 90° Ch5: 0° Ch6: 0° Ch7: 0° Ch8: 0° |
| Phase setting 4 Ch1: 0° Ch2: 180° Ch3: 0° Ch4: 90° Ch5: 0° Ch6: 0° Ch7: 0° Ch8: 0° | Phase setting 5 Ch1: 90° Ch2: 0° Ch3: 90° Ch4: 0° Ch5: 0° Ch6: 0° Ch7: 0° Ch8: 0° | Phase setting 6 Ch1: 0° Ch2: 90° Ch3: 0° Ch4: 180° Ch5: 0° Ch6: 0° Ch7: 0° Ch8: 0° |

Table 15 – phase settings used in order to achieve a more homogeneous B_1^+ field.

Images of the region of interest resulting from *in vivo* B_1^+ shimming using phase settings described in Table 15 are shown in Figure 53 (TR = 8.6 ms, TE = 4 ms, in plane resolution: $0.4 \times 0.4 \text{ mm}^2$, slice thickness: 5 mm, matrix: 512×512). The phase setting 3 showed an overall better SNR (brighter image) and less RF destructive interference.

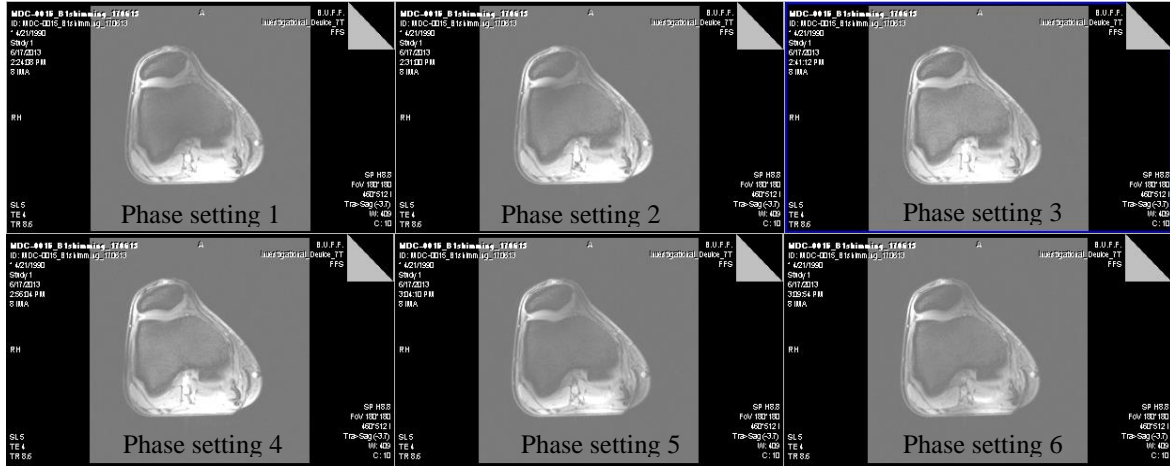


Figure 53 – GRE images from the region of interest using different phase setting of Table 15.

Using the phase sitting 3, the image quality is also improved for other knee anatomies as can be seen on Figure 54, comparing a scan without phase setting and a scan with phase setting 3.

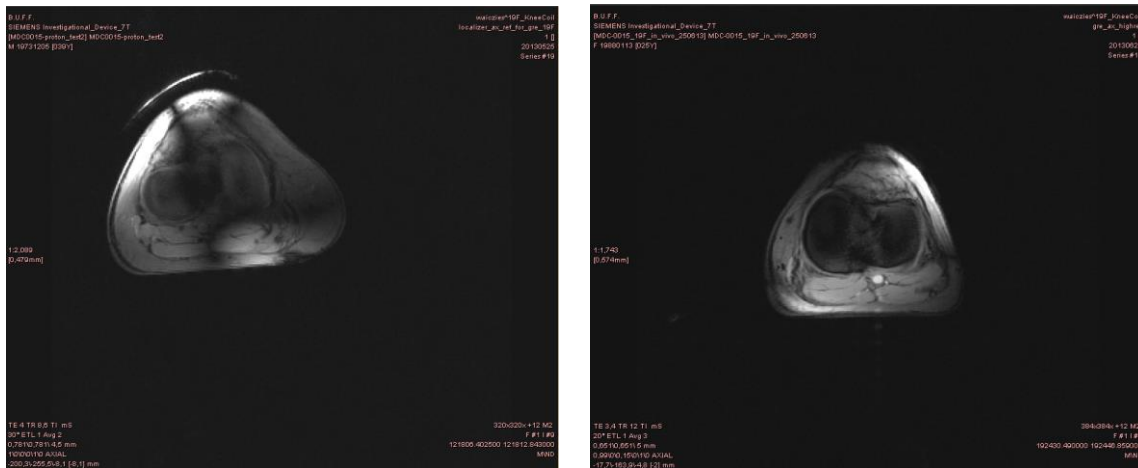


Figure 54 – The left image was acquired without any phase setting and destructive interference of short wavelength of the RF field can be observed. The right image used phase setting 3 and a more homogeneous B_1^+ distribution can be observed.

5.1.1. Proton and fluorine imaging

A slice of high resolution proton images (TR = 12 ms, TE = 3.4 ms, in plane resolution: $0.7 \times 0.7 \text{ mm}^2$, slice thickness: 5 mm, matrix: 384×384), and fluorine images (TR = 90 ms, TE = 1.3 ms, in plane resolution: $2 \times 2 \text{ mm}^2$, slice thickness: 5 mm, matrix: 128×128) of a subject's knee with topical applied flufenamic acid containing NSAID ointment on the nearby skin are shown on Figure 55.

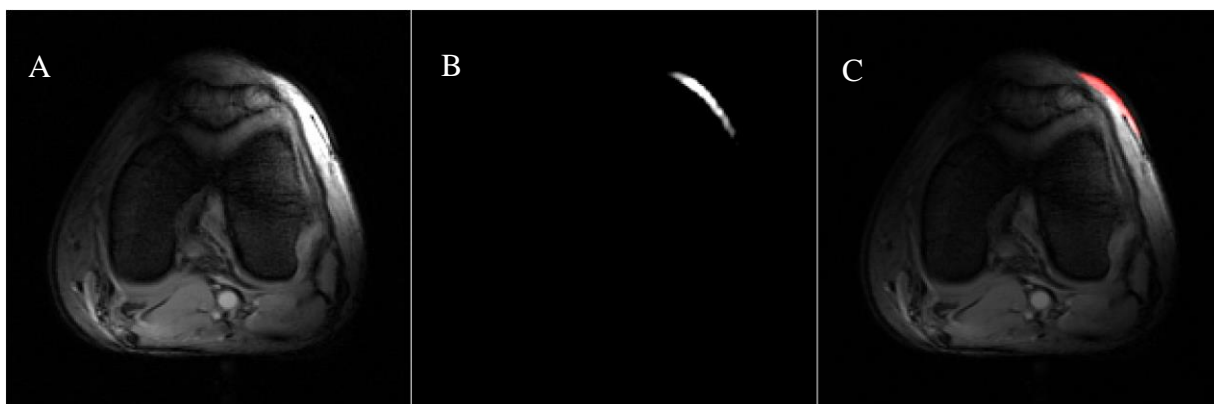


Figure 55 – A: High resolution proton image ($0.7 \times 0.7 \times 5 \text{ mm}$). B: high resolution fluorine image ($2 \times 2 \times 5 \text{ mm}$). C: combined $^1\text{H}/^{19}\text{F}$ image.

5.9. *In vivo* ^{19}F Spectroscopy

Results of *in vivo* unlocalized ^{19}F spectroscopy of the flufenamic acid contained NSAID ointment topically applied to volunteers' skin near by the knee are shown in Table 16 and plotted on Figure 56.

There was no signal on the spectrogram of the spectroscopy performed with SPECIAL voxel placed inside the knee beneath the skin where the NSAID was topically applied.

| Subject 1 (0.621 mmol of fluf. acid) | | Subject 2 (1.028 mmol of fluf. acid) | |
|--------------------------------------|---|--------------------------------------|---|
| Time (min) | Signal magnitude a.u. ($\times 10^{-5}$) | Time (min) | Signal magnitude a.u. ($\times 10^{-5}$) |
| 0 | 1.31 | 0 | 1.93 |
| 16 | 1.46 | 31 | 2.06 |
| 28 | 1.61 | 132 | 1.80 |
| 46 | 1.68 | 155 | 1.84 |
| 65 | 1.75 | 172 | 1.93 |

Table 16 – ^{19}F spectroscopy over time of the two subjects who applied topically the fluorine containing ointment on the skin near the knee.

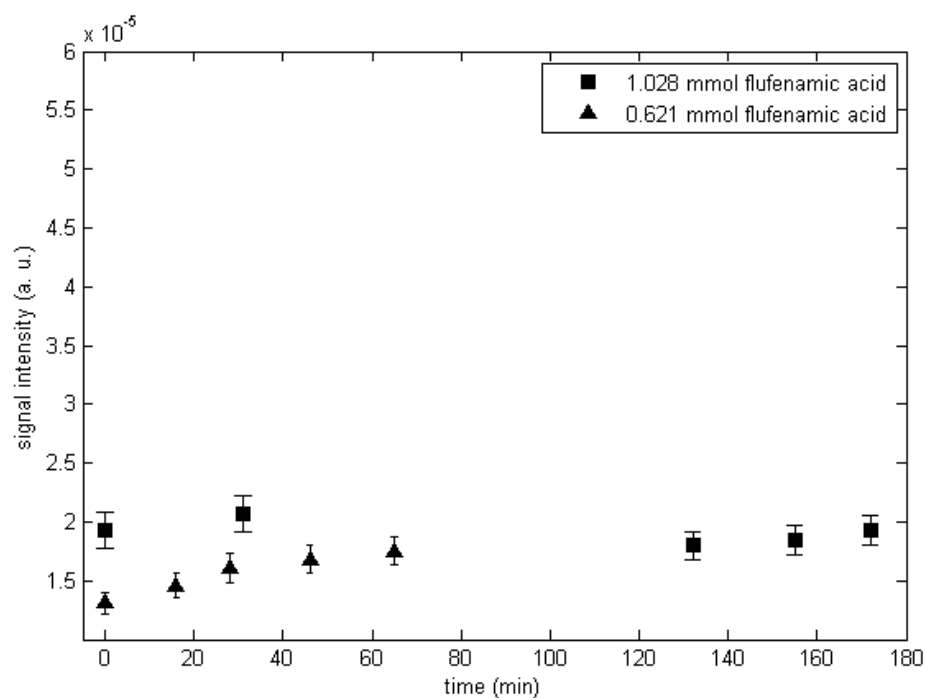


Figure 56 – graphic visualization of data of the Table 16.

6. DISCUSSION

In this project, a knee coil tuned to proton and to fluorine frequencies was constructed in order to access the dynamics of a fluorine contained NSAID ointment, from its application in the skin to the site of inflammation in knees suffering from rheumatoid arthritis. In this section, results obtained in the previous section are discussed.

6.1. Coil performance

The coil consisted of two bent anterior parts that easily cover the anterior part of an average knee and one lower part that was designed to support an average knee in a bent position; this offers better comfort than a plane design for MRI examining subjects. The three parts of the coils are made by eight loop elements to cover all the region of interest, since surface coils have reduced field of view of approximately its diameter.

Cable traps built to suppress the induced unbalanced currents in the feeding coaxial cables of each channel show a performance ranged from -13 dB to -20 dB. In the worst case, 5% of the unbalanced shield current is not attenuated, hence the cable traps can be considered to have a reasonable performance.

The reflection coefficients (S_{ii}) of each coil element were situated below -30 dB, which means that only 0.1% of the power is reflected back. This result show that tuning and matching of the coil was well performed and little loss occurs. This is important for coil performance since loss in reflection will result in less available power to generate the B_1^+ field to excite the spins. On the other hand, the transmission coefficients (S_{ij}) of the elements of the same coil parts showed a variation from -16 dB to -25 dB meaning that in the worst case 2.5% of the power delivered to an element is lost into another. This is an acceptable result since it does not translate into a significant loss. By changing the capacitance of the tuning, matching and decoupling of the trim capacitors, the coil could be easily adapted to various subjects and to the phantom without further capacitance changes in the conductor shortening capacitors.

The ratio between loaded and unloaded Q , of all coil elements, lies below 0.5. This is a desired result since Q_L/Q_{uL} below 0.5 indicates the dominance of sample noise, and under this situation an optimum SNR could be achieved.

6.2. B_1^+ mapping comparison

The simulated and measured B_1^+ maps patterns showed a significant agreement. It is important to refer that the phantom used in the measurements was constructed by colleagues at B.U.F.F. and was aimed to measure temperature changes in RF heating experiments, thus it has three holes along its extension for the insertion of thermometers. This fact caused artifacts in B_1^+ patterns of elements 1 and 2, since the holes are considered singularities in the Bloch algorithm when unwrapping phase.

The comparison of maximum values of the measured and the simulated B_1^+ (Table 8), revealed that the measurements are 15% to 53% less than the simulations, with a higher loss at fluorine channels. An unexpected gain of 20% in B_1^+ value was found in channel 1 which led to a further analysis of B_1^+ map of this channel. It was found that the maximum measured B_1^+ value of channel 1 was located in a region far away from the coil, where a hole for a thermometer is located, Figure 57. The actual maximum B_1^+ value produced by the coil is approximately $27 \mu T/\sqrt{kW}$, which compared to simulated B_1^+ , is 17% less.

With the corrected value for channel 1, the measured maps for proton channels showed an extra loss of $21.5 \pm 7.6\%$ compared to simulated maps, despite the loss correction made in Table 7. On this table S_{ii} values for channels 1 and 2 were not registered, but since these channels were tuned and matched to the proton frequency, S_{ii} should not be higher than -15 dB, thus the B_1^+ value correction with S-parameters should not produce significant difference. The extra losses could be explained by further unknown losses in the MR system.

The phantom used in the B_1^+ mapping measurements did not contain fluorine compounds, thus, the B_1^+ maps of fluorine elements were acquired in proton frequency and then extrapolated to fluorine frequency by correcting with S-parameters. Also, the S-parameters were acquired in the laboratory and not inside the scanner; therefore they are just an

approximation of the actual S-parameters values of the mapping measurement. This fact, plus further losses that occur in the MR system could explain the relatively high difference, $47.8 \pm 9.2\%$, between measured and simulated ^{19}F channels.

In this experiment, the validity of the simulation could be accepted by reasonable qualitative and quantitative agreement between measured and simulated B_1^+ maps of the proton channels. On the other hand, despite the qualitative agreement, relatively higher quantitative difference was found in fluorine channels, due to the fact that there was no fluorine containing phantom available to make a proper ^{19}F B_1^+ mapping, this fact should not deter the validation of the simulations, which gives credibility of SAR simulations.

A more accurate B_1^+ mapping for the dual tuned knee coil could be made, by using a uniform proton containing phantom for ^1H channels and a uniform fluorine containing phantom for ^{19}F measurements. Also, the simulations should reproduce the exact positioning, size and dielectric properties of the phantom in MR experiments to achieve a better comparison.

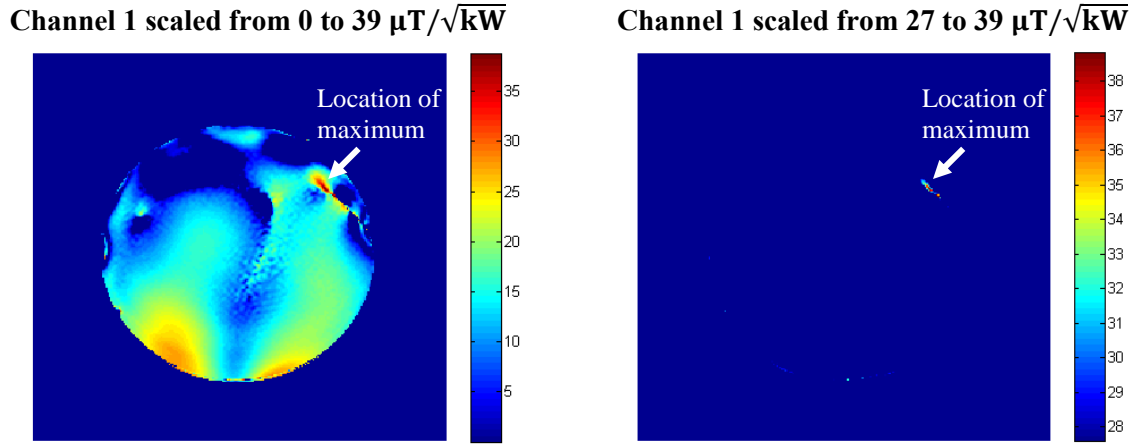


Figure 57 – Left: B_1^+ map of channel 1 scaled from 0 to 39 $\mu\text{T}/\sqrt{\text{kW}}$. Right: B_1^+ map of channel 1 scaled from 27 to 39 $\mu\text{T}/\sqrt{\text{kW}}$, it shows that the maximum B_1^+ value is not located in the expected region next to the channel 1, instead it is located in a far region from the channel 1 where a hole for insertion of a thermometer is placed. At approximately 27 $\mu\text{T}/\sqrt{\text{kW}}$ there is no signal left in the region next to channel 1, thus this value can be said to be the actual maximum B_1^+ value produced by channel 1.

6.3. SAR evaluation

For input power of 1 W to all the channels, 10 g averaged SAR for phase setting 3 was found to be 0.306 W/kg at 279.5 MHz (fluorine frequency) and 0.375 W/kg at 297.0 MHz (proton frequency). As the limit defined by IEC for 10g SAR at body extremity is 20 W/kg, a power increase until as high as 53 W for the coil at this phase setting (resulting in SAR value of 19.9 W/kg) will still stay within the limit of IEC guidelines.

Since different phase and amplitude settings of the power at each port affects the SAR, the worst case SAR given by MRI toolkit of SEMCAD X could be used, for safety issues, as reference for delimitation of the RF power in the coil plug.

It is also important to refer that the SAR calculations are made without power loss that occurs in real MR scans, thus, in real-life, the SAR values would not exceed the expected value from the simulations.

6.4. T_1 , T_2 and concentration curve

Different T_1 and T_2 values were found for 100% flufenamic acid containing NSAID ointment sample and 50% flufenamic acid containing NSAID ointment + 50% non-fluorine containing ointment sample. This is an expected result, since the molecular environment was modified with the introduction of non-fluorine containing ointment. This also explains different concentration curve slopes of these two samples.

6.5. *In vivo* imaging and ^{19}F spectroscopy

In vivo high spatial resolution proton images ($\text{TR} = 12 \text{ ms}$, $\text{TE} = 3.4 \text{ ms}$, in plane resolution: $0.7 \times 0.7 \text{ mm}^2$, slice thickness: 5 mm, matrix: 384×384) with phase setting 3 showed homogenous image quality and contrast. The Overlapping of ^{19}F image ($\text{TR} = 90 \text{ ms}$, $\text{TE} = 1.3 \text{ ms}$, in plane resolution: $2 \times 2 \text{ mm}^2$, slice thickness: 5 mm, matrix: 128×128) and ^1H image allows visualization and localization of fluorine contained NSAID ointment. This is of a major importance for *in vivo* drug tracking, which permits the sight of ^{19}F

contained NSAID localization within the body, if drug penetration occurs and if the penetrated quantity allows the detection.

In vivo ^{19}F spectroscopy performed with two healthy subjects with topically applied flufenamic acid contained NSAID in the skin near the knee didn't show signal decrease compared to the initial signal (Table 16 and Figure 56), which was originally expected to occur if any quantity of NSAID would be skin absorbed. In fact, non-localized spectroscopy excites all the ^{19}F nuclei within the FOV, which included regions outside and inside the body, in this way the spectroscopy made is inconclusive.

On the other hand the spectroscopy performed to subject 2 with SPECIAL voxel placed inside the knee beneath skin area where topical NSAID was applied did not show presence of fluorine after 172 minutes of beginning of the scanning session. This result shows that either it did not occurred any skin absorption of the topically applied NSAID at depth of the placed SPECIAL voxel within the scanning time, or the absorption occurred, but the absorbed quantity could be too low to be detected.

Further *in vivo* studies could be performed using voxel spectroscopies, one placed outside the knee on top of the area where NSAID is applied and other placed inside the knee beneath application area. This should be performed with patients with rheumatoid arthritis in the knee and also with health volunteers. In this way, the absence of fluorine signal in the *in vivo* experiment performed for this work could also be checked if was due to the inexistence of the inflammation site for NSAID penetration. The absorption of NSAID could also be monitored for longer periods, such as days, instead of just a few hours, as it was used in this study. Therefore, an accumulative absorption of the NSAID could be evaluated.

7. CONCLUSION

The eight channel dual tuned knee array coil constructed for the present thesis for the use at 7.0 T ultrahigh magnetic field showed good performance evidenced by its low reflection and transmission coefficients (<-30 dB and <-16 dB respectively) and noise dominant Q ratio, which enounces SNR gain.

The performed EM simulations with a phantom showed reasonable qualitative and quantitative agreement with the experiment results for proton channels validating the reliability of the SAR calculations for a human model, which give an estimation of the deposited RF power in the tissue.

High spatial resolution images were acquired with this coil for proton (0.7×0.7 mm² in plane resolution and 5 mm slice thickness) and for fluorine (2×2 mm² in plane resolution and 5 mm slice thickness \times 5 mm). After an *in vivo* B₁⁺ shimming session, images presented an increased quality since the RF destructive interference was attenuated. These parameters are important for knee imaging due to small structures around this joint.

In vivo unlocalized ¹⁹F spectroscopy that aimed to observe and to quantify the skin absorption of flufenamic acid contained NSAID showed inconclusive results. And the spectroscopy performed with a SPECIAL voxel placed inside the knee did not show any fluorine signal, either due to non-absorption of the NSAID or the absorbed quantity was too low to be detected.

Further improved *in vivo* experiments could be carried out using the dual tuned ¹H/¹⁹F knee coil in the study of the effectiveness of penetration and action of NSAIDs within patients with rheumatoid arthritis (RA) in the knee. These experiments could be performed using two voxel, one inside and one outside the knee, for ¹⁹F spectroscopy, in healthy and RA patients for longer monitoring times.

8. REFERENCES

- [1] Rheumatoid arthritis, (2012).
- [2] S.B. Abramson, Mechanisms of action of nonsteroidal anti-inflammatory drugs and therapeutic considerations., *Bulletin of the Hospital for Joint Diseases Orthopaedic Institute*. 50 (1990) 107–15.
- [3] C.A. Heyneman, C. Lawless-Liday, G.C. Wall, Oral versus topical NSAIDs in rheumatic diseases: a comparison., *Drugs*. 60 (2000) 555–74.
- [4] A.R. Brewer, B. McCarberg, C.E. Argoff, Update on the use of topical NSAIDs for the treatment of soft tissue and musculoskeletal pain: a review of recent data and current treatment options., *The Physician and Sportsmedicine*. 38 (2010) 62–70.
- [5] R. Buchbinder, Topical NSAIDs provide effective relief of acute musculoskeletal pain compared to placebo, with no increase in risk of adverse effects., *Evidence-based Medicine*. 15 (2010) 177–8.
- [6] L.S. Simon, Do topical NSAIDs work?, *Nature Clinical Practice. Rheumatology*. 4 (2008) 458–9.
- [7] L. Mason, R.A. Moore, J.E. Edwards, S. Derry, H.J. McQuay, Topical NSAIDs for chronic musculoskeletal pain: systematic review and meta-analysis., *BMC Musculoskeletal Disorders*. 5 (2004) 28.
- [8] J.J. Escobar-Chávez, V. Merino-Sanjuán, M. López-Cervantes, Z. Urban-Morlan, E. Piñón-Segundo, D. Quintanar-Guerrero, et al., The tape-stripping technique as a method for drug quantification in skin., *Journal of Pharmacy & Pharmaceutical Sciences : a Publication of the Canadian Society for Pharmaceutical Sciences, Société Canadienne Des Sciences Pharmaceutiques*. 11 (2008) 104–30.
- [9] A. Zesch, H. Schaefer, Penetration kinetics of four drugs in the human skin. Influences of various pharmaceutical vehicles on penetration in vitro., *Acta Dermato-venereologica*. 54 (1974) 91–7.
- [10] G.N.HOLLAND, P.A.B.W.S. HINSHAW, COMMUNICATIONS 19F Magnetic Resonance Imaging, *Journal of Magnetic Resonance*. 136 (1977) 133–136.
- [11] D.W. McRobbie, E.A. Moore, M.J. Graves, M.R. Prince, *MRI from Picture to Proton*, Cambridge University Press, 2007.

- [12] J. Chen, G.M. Lanza, S. a Wickline, Quantitative magnetic resonance fluorine imaging: today and tomorrow., Wiley Interdisciplinary Reviews. Nanomedicine and Nanobiotechnology. 2 (2010) 431–40.
- [13] F. Schick, Whole-body MRI at high field: technical limits and clinical potential., European Radiology. 15 (2005) 946–59.
- [14] J. Mispelter, M. Lupu, A. Briguet, Nmr Probeheads for Biophysical And Biomedical Experiments: Theoretical Principles And Practical Guidelines, Imperial College Press, 2006.
- [15] M.A. Brown, R.C. Semelka, MRI: Basic Principles and Applications, Wiley, 2003.
- [16] F.D. Hockett, K.D. Wallace, A.H. Schmieder, S.D. Caruthers, C.T.N. Pham, S.A. Wickline, et al., Simultaneous dual frequency 1H and 19F open coil imaging of arthritic rabbit knee at 3T., IEEE Transactions on Medical Imaging. 30 (2011) 22–7.
- [17] P. Suetens, Fundamentals of Medical Imaging, Cambridge University Press, 2009.
- [18] E.M. Haacke, R.W. Brown, M.R. Thompson, R. Venkatesan, Magnetic Resonance Imaging: Physical Principles and Sequence Design, Wiley, 1999.
- [19] R.R. Edelman, J. V. Crues, J.R. Hesselink, M.B. Zlatkin, Clinical Magnetic Resonance Imaging Online: Access to Continually Updated Online Reference, Elsevier Science Health Science Division, 2005.
- [20] D. Weishaupt, V.D. Köchli, B. Marincek, How does MRI work?: An Introduction to the Physics and Function of Magnetic Resonance Imaging, Springer, 2008.
- [21] J.T. Bushberg, J.A. Seibert, E.M. Leidholdt, J.M. Boone, The Essential Physics for Medical Imaging, (2002) 933.
- [22] J.P. Hornak, The Basics of MRI, Interactive Learning Software, Henrietta, NY, n.d.
- [23] WebElements: the periodic table on the web, (n.d.).
- [24] R.Y. Kwong, Cardiovascular Magnetic Resonance Imaging, Springer, 2008.
- [25] J.D. Jackson, Classical Electrodynamics, Wiley, 1998.
- [26] D.I. Hoult, The principle of reciprocity in signal strength calculations - A mathematical guide, Concepts in Magnetic Resonance. 12 (2000) 173–187.
- [27] a M. Blamire, The technology of MRI--the next 10 years?, The British Journal of Radiology. 81 (2008) 601–17.

- [28] M. V Knopp, Ultra-High Field Clinical Brain MR Imaging : Challenge and Excitement, Proc. Intl. Soc. Mag. Reson. Med. 17 (2009) 2009.
- [29] R. Burgess, Magnetic Resonance Imaging at Ultrahigh Field: Implications for Human Neuroimaging, (2004) 237.
- [30] A. Lutti, F. Dick, M.I. Sereno, N. Weiskopf, Using high-resolution quantitative mapping of R1 as an index of cortical myelination., NeuroImage. (2013).
- [31] IEC 60601-2-33 ed3.0 - Medical electrical equipment - Part 2-33: Particular requirements for the basic safety and essential performance of magnetic resonance equipment for medical diagnosis, (2010).
- [32] P.A. Bottomley, Turning up the heat on MRI., Journal of the American College of Radiology : JACR. 5 (2008) 853–5.
- [33] S. Webb, The Physics of Medical Imaging, CRC Press, 2010.
- [34] P.B. Roemer, W.A. Edelstein, C.E. Hayes, S.P. Souza, O.M. Mueller, The NMR phased array., Magnetic Resonance in Medicine : Official Journal of the Society of Magnetic Resonance in Medicine / Society of Magnetic Resonance in Medicine. 16 (1990) 192–225.
- [35] A. Ok, Design, Construction and Evaluation of a Flexible Carotid Coil for MRI at 7.0 T, 2012.
- [36] A. Hassan, I. Elabyed, J. Mallow, T. Herrmann, J. Bernarding, A. Omar, Optimal geometry and capacitors distribution of 7T MRI surface coils, Microwave Conference (EuMC), 2010 European. (2010) 1437–1440.
- [37] M.A. Lopez, E. Al., Overlap Decoupling in Hole-Slotted Arrays, Int. Soc. Mag. Reson. Med. (2010).
- [38] J. Wang, A novel method to reduce the signal coupling of surface coils for MRI., Proc. Int. Soc. Mag. Reson. Med. 3 (1996) 1434.
- [39] J.J. Carr, Secrets of RF Circuit Design (Tab Electronics), McGraw-Hill/TAB Electronics, 2000.
- [40] S.J. Orfanidis, Electromagnetic Waves and Antennas, (2008).
- [41] Building RF Surface Coils for MRI, (n.d.).
- [42] X. Hu, D.G. Norris, Advances in high-field magnetic resonance imaging., Annual Review of Biomedical Engineering. 6 (2004) 157–84.

- [43] SPEAG, SEMCAD X Manual, 14.8.3 ed., Schmid & Partner Engineering AG, 2012.
- [44] I. Foundation, Virtual Family flyer, (n.d.).
- [45] L.I. Sacolick, F. Wiesinger, I. Hancu, M.W. Vogel, B1 mapping by Bloch-Siegert shift., *Magnetic Resonance in Medicine : Official Journal of the Society of Magnetic Resonance in Medicine / Society of Magnetic Resonance in Medicine*. 63 (2010) 1315–22.
- [46] V. Mlynárik, G. Gambarota, H. Frenkel, R. Gruetter, Localized short-echo-time proton MR spectroscopy with full signal-intensity acquisition., *Magnetic Resonance in Medicine : Official Journal of the Society of Magnetic Resonance in Medicine / Society of Magnetic Resonance in Medicine*. 56 (2006) 965–70.